

# Design of a Nanometer Beam Size Monitor for ATF2

Taikan Suehara <sup>a</sup>, Masahiro Oroku <sup>b</sup>, Takashi Yamanaka <sup>b</sup>,  
Hakutaro Yoda <sup>b</sup>, Tomoya Nakamura <sup>b</sup>, Yoshio Kamiya <sup>a</sup>,  
Yosuke Honda <sup>c</sup>, Tatsuya Kume <sup>d</sup>, Toshiaki Tauchi <sup>e</sup>,  
Tomoyuki Sanuki <sup>f</sup>, and Sachio Komamiya <sup>b</sup>

<sup>a</sup>*ICEPP, The Univ. of Tokyo, 7-3-1 Hongo, Bunkyo, Tokyo, 113-0033, Japan*

<sup>b</sup>*Dept. of Physics, The Univ. of Tokyo, 7-3-1 Hongo, Bunkyo, Tokyo, 113-0033, Japan*

<sup>c</sup>*Accelerator Laboratory, KEK, 1-1 Oho, Tsukuba, Ibaraki, 305-0801, Japan*

<sup>d</sup>*Applied Research Laboratory, KEK, 1-1 Oho, Tsukuba, Ibaraki, 305-0801, Japan*

<sup>e</sup>*Institute of Particle and Nuclear Studies, KEK, 1-1 Oho, Tsukuba, Ibaraki, 305-0801, Japan*

<sup>f</sup>*Dept. of Physics, Tohoku Univ., 6-3 Aoba, Aramaki, Aoba, Sendai, Miyagi, 980-8578, Japan*

---

## Abstract

We developed an electron beam size monitor for extremely small beam sizes. It uses a laser interference fringe for a scattering target with the electron beam. Our target performance is  $< 2$  nm systematic error for 37 nm beam size and  $< 10\%$  statistical error in a measurement using 90 electron bunches for 25 - 6000 nm beam size. A precise laser interference fringe control system using an active feedback function is incorporated to the monitor to achieve the target performance. We describe an overall design, implementations, and performance estimations of the monitor.

*Key words:* Beam size monitor, Beam focusing, ILC, ATF2, Shintake monitor

*PACS:* 29.27.Fh, 41.85.Ew, 07.60.Ly, 13.60.Fz, 29.40.Mc, 07.10.Fq

---

---

*Email address:* `suehara@icepp.s.u-tokyo.ac.jp` (Taikan Suehara).

# 1 Introduction

## 1.1 Principles

Nanometer focusing of the electron and positron beams is one of the key technologies to realize the coming International Linear Collider (ILC)[1]. The beam size at the ILC interaction point (IP) is designed to be 640 nm (horizontal) by 5.7 nm (vertical) to achieve the required integrated luminosity of  $500 \text{ fb}^{-1}$  within first four years of operation. To achieve these beam sizes, especially 5.7 nm vertical beam size, precise tuning of position and field strength for magnets in the final focus line is required. An IP beam size monitor is necessary for the tuning and for demonstrations of the nanometer focusing.

For intense electron<sup>1</sup> beams, movable fine wire targets are widely used to acquire the beam size. Electron beams scatter with the wire targets, emitting photons which can be captured by gamma detectors. Metal and carbon wires down to several  $\mu\text{m}$  thickness have been used for the targets. However, for sub- $\mu\text{m}$  beam size, electron beams are so intense that they break the wires[2], thus material wires cannot be utilized.

To avoid the heat destruction, laser beams can be alternatives of the material wires for intense electron beams. Since laser beams scatter with electron beams emitting inverse-Compton scattered photons, they can be used as similar to material wires (laser-wire). Minimum observable electron beam size by a laser-wire is determined by the laser spot size, which is limited to around its wavelength by diffraction limit. Therefore, sub-100 nm beam size measurement needs deep-UV lasers, which is not available now.

For sub-100 nm electron beam size, a laser interferometer technology, called Shintake monitor[3a–b] can be utilized. Figure 1 shows a schematic of the monitor. A laser beam is split in two and the split beams cross at the focal point of the electron beam. In the intersected area of the two laser beams, the electromagnetic fields of the two laser beams form a standing wave (interference fringe). Probability of the Compton scattering varies by the phase of the standing wave where the electrons pass through, that is, the scattering probability is high for electrons passing through the top of the fringe, and is low for those passing through the bottom of the fringe. Note that the standing wave of the magnetic and the electric field has opposite phase, but for the high energy electron beam, effect of the electric field is strongly suppressed if we choose the magnetic field direction perpendicular to the electron beam direction. The detailed discussion is appeared in [4].

---

<sup>1</sup> Positrons can be treated as similar.

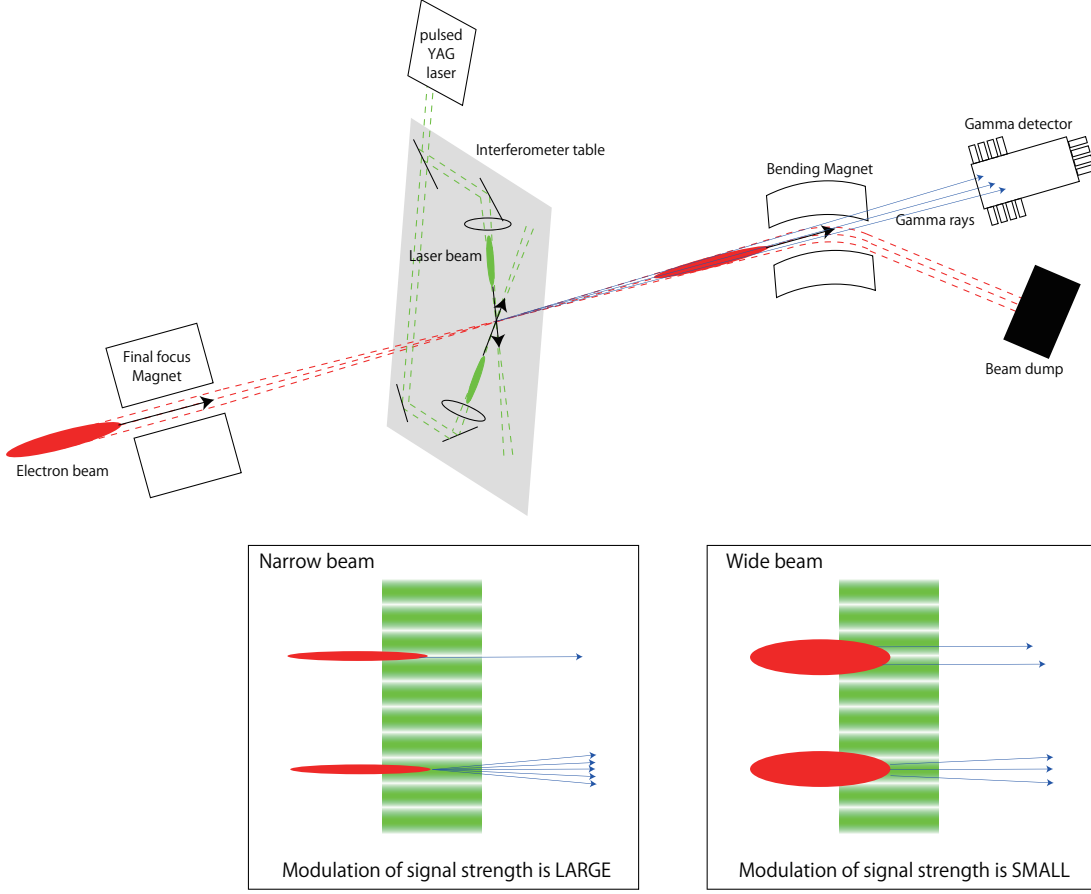


Fig. 1. A schematic of the laser interferometer (Shintake monitor).

For electron beams well focused compared to the fringe spacing, all electrons in the beam pass through almost the same phase of the fringe. This results in a large modulation of the Compton scattering signals monitored at a gamma detector downstream of the electron beam line. On the contrary, for dispersed electron beams, electrons pass through wide variety of phases of the fringe, thus the modulation of the signals is low. By calculation of the magnetic field described in [3b], electron beam size  $\sigma$  is related to the modulation of the monitored Compton signal  $M = |(N_+ - N_-)/(N_+ + N_-)|$  (where  $N_+$  is the maximum signal intensity of the modulation and  $N_-$  is the minimum signal intensity of the modulation) as,

$$M = |\cos 2\phi| \exp \left[ -2(k_{\perp} \sigma)^2 \right] \quad (1)$$

where  $\phi$  is the crossing angle (half angle) of the two laser beams and  $k_{\perp} = k \sin \phi$  is the wavenumber along the direction perpendicular to the fringe.  $M = 5 - 90\%$  can be used for the beam size measurement, thinking of various measurement fluctuation. Observable beam size range of the monitor is varied by  $k_{\perp}$ , which is determined by laser wavelength and crossing angle, as shown in Fig. 2. Beam sizes down to  $< 10$  nm is observable by this method if a UV

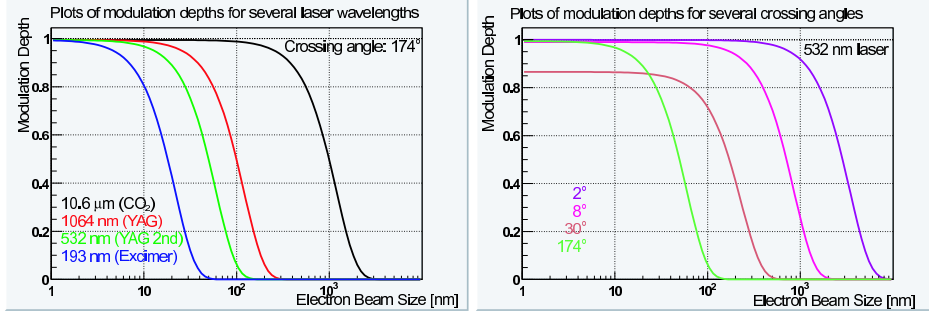


Fig. 2. Relation between electron beam sizes and modulation depths. Left: comparison between several laser wavelengths. Right: comparison between several crossing angles.

laser with a large crossing angle is selected.

## 1.2 Modulation Measurement

Practically, accelerated electron beam comes in bunches, and we introduce laser pulses to the IP to interact with the electron bunches. We obtain Compton signal strength from a bunch (or several bunches) at certain phase of the laser interference fringe, and obtain signal strength from another bunch (or other bunches) at another phase. Repeating that results in a modulation spectrum, which is a plot of Compton signal strengths for fringe phases.

Figure 3 (upper) shows a sample modulation spectrum. Each point stands for a signal intensity in a bunch, including measurement errors such as power fluctuation, phase fluctuation and background fluctuation. To obtain good modulation spectrum and thus good resolution of beam size measurements, we need to suppress these error factors.

Shintake monitor is firstly realized in Final Focus Test Beam experiment[5a–b], constructed in Stanford Linear Accelerator Center. Figure 3 (lower) shows an example of the modulation spectrum obtained in the FFTB Shintake monitor[6]. In the FFTB Shintake monitor, fringe phase at the electron beam was controlled by shifting the path of the electron beam by a steering magnet because they had no phase control feature in their laser optical system. In our monitor, the laser fringe phase is monitored and controlled instead of shifting electron beam path, as described in Section 4.

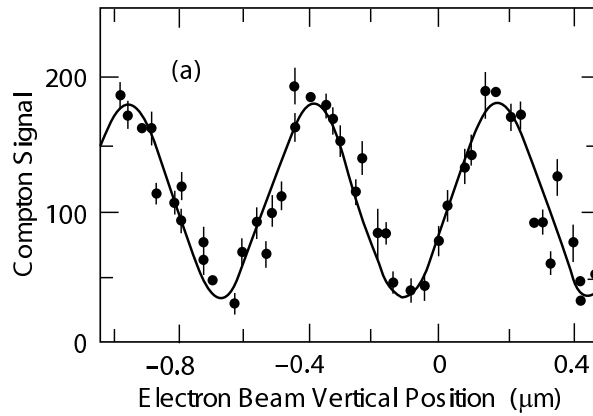
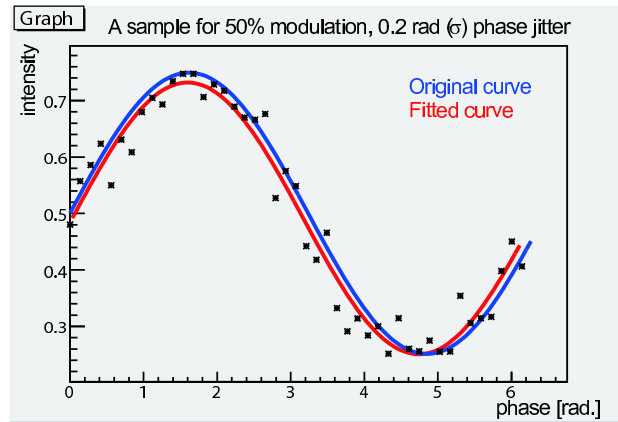


Fig. 3. Upper: a sample modulation spectrum produced by a toy Monte Carlo simulation. 0.2 radian RMS phase fluctuation is introduced in each point, and the fluctuation causes deviation of the sine fitting (red line) from the original curve (blue line). Lower: a modulation spectrum measured by the FFTB Shintake monitor.

Beam Energy	1.3 GeV
Normalized Emittance $\gamma\epsilon_x$	$3 \times 10^{-6}$ m·rad
Normalized Emittance $\gamma\epsilon_y$	$3 \times 10^{-8}$ m·rad
Bunch Population	$0.5 \times 10^{10}$
Bunch Length	5 mm (17 psec)
Repetition Rate	1.56 Hz
Focal Length $L^*$	1.0 m
IP Beta Function $\beta_x^*$	4.0 mm
IP Beta Function $\beta_y^*$	0.1 mm
IP Beam Size $\sigma_x^*$	2.8 $\mu\text{m}$
IP Beam Size $\sigma_y^*$	37 nm

Table 1  
Major specifications of ATF & ATF2.

## 2 Layout and Structure

### 2.1 Overall Structure

Our monitor is designed as the IP<sup>2</sup> beam size monitor of Accelerator Test Facility 2 (ATF2)[7], a final focus test facility for the ILC. ATF2 is being constructed downstream an ILC dumping ring test facility, Accelerator Test Facility (ATF) at High Energy Accelerator Research Organization (KEK). Major specifications of ATF and ATF2 are shown in Table 1. Design beam size at the ATF2 IP is  $\sigma_y^* = 37$  nm,  $\sigma_x^* = 2.8$   $\mu\text{m}$ . Since the monitor is also used as a beam tuning tool to obtain small beam size, target beam size of the monitor is 25 nm to 6  $\mu\text{m}$  for  $\sigma_y^*$ , and 2.8 to 100  $\mu\text{m}$  for  $\sigma_x^*$ . We implement a Shintake monitor with several crossing angles for  $\sigma_y^*$  measurements, and a laser-wire for  $\sigma_x^*$  measurements, incorporated in a single IP beam size monitor system.

Figure 4 shows a schematic layout of the monitor. It consists of a main optical table, a gamma detector with collimators, a laser source with a transport line, and control electronics. The main optical table is installed just on the IP to form laser interference fringes. Laser photons are supplied from a laser located in the laser & electronics hut, transported via the laser transport line. The electron beam is focused at the IP by the final focusing magnets. After

---

<sup>2</sup> Although ATF2 causes no interaction at the focal point, we call it ‘IP’ to clarify a relation to the ILC.

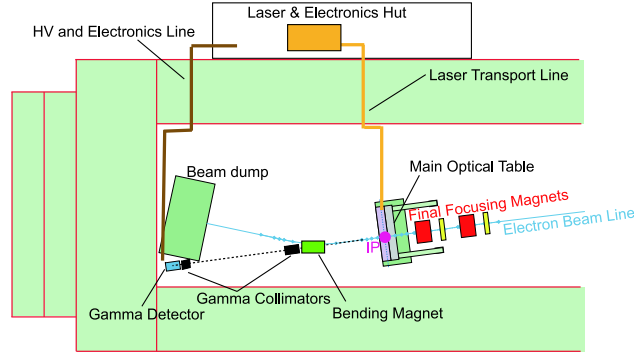


Fig. 4. Schematic layout of the monitor and around the ATF2 IP.

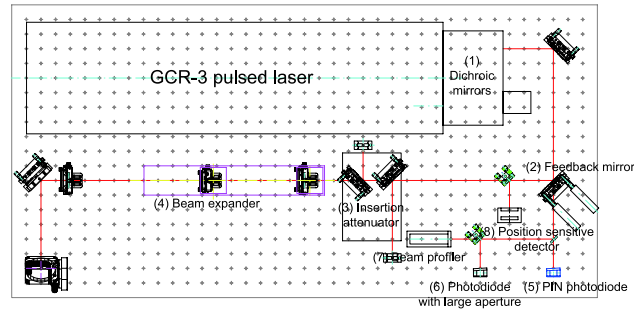


Fig. 5. Layout of the laser table. Red lines show laser optical paths.

the IP, the electron beam is bended at the bending magnet and sent to the beam dump. Compton photons are not bended by the bending magnet, and go straight to the gamma detector through apertures of the gamma collimators.

## 2.2 Laser and Main Optical Table

To obtain enough number of photons, we need high density of laser photons at the IP. We use a high power Q-switched pulsed laser whose peak power is up to 40 MW. Pulse length of the laser is about 8 nsec (FWHM), which is much longer than the electron bunch length 17 psec. The laser output is triggered by a electron beam signal observed by a beam position monitor in the ATF dumping ring. Q-switch timing jitter of the laser is measured to be about 300 psec, which causes no significant density fluctuation of photons interacted with an electron beam. Wavelength of the laser is 532 nm (YAG 2nd harmonics) to obtain good sensitivity for the monitor at 37 nm electron beam size (see Fig. 2). Spectral width of the laser is  $< 90$  MHz, narrow enough to obtain good fringe contrast at the IP.

Figure 5 shows a layout of the laser table. The purpose of the table is to adjust and monitor characteristics of the laser beam to be sent to the main optical table. A 532 nm monochromatic laser beam is created by the laser and dichroic mirrors(1). A feedback mirror(2) is a partial( $\sim 95\%$ ) reflecting mirror with



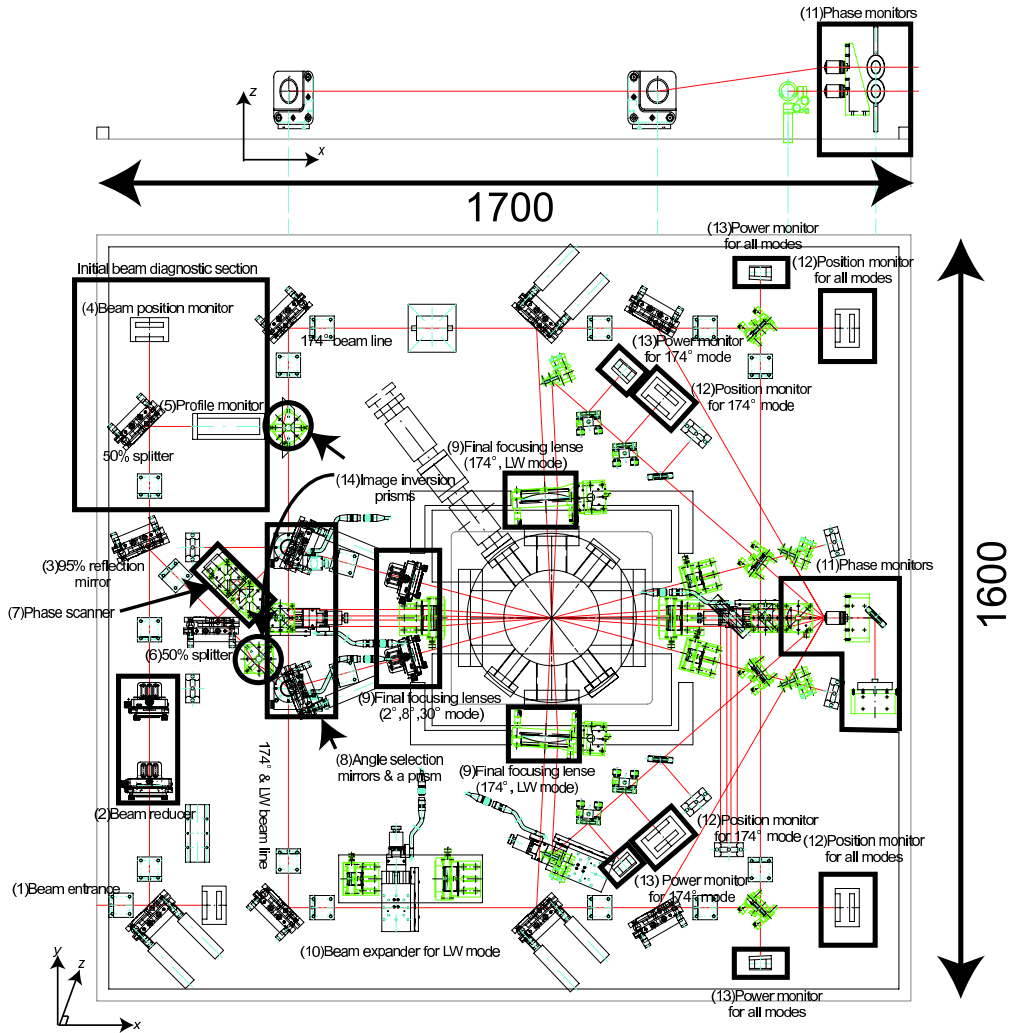


Fig. 6. Layout of the main optical table of the monitor. Beam height from the table top is  $z = 100$  mm for all the optical components except the phase monitor, shown in the upper figure.

actuators used for laser beam position stabilization. An insertion attenuator(3) can provide low power laser paths for an alignment. A beam expander(4), which consists of three lenses, magnifies a laser spot size to reduce a laser beam dispersion angle in the transport line. The spot size is continuously adjustable by shifting positions of the three lenses. In the current design, the spot size at the transport line is  $7.0 \text{ mm}^3$ . Components of (5) to (8) are to monitor timings, powers, profiles, and positions of laser pulses, shot by shot.

The laser photons are delivered to the main optical table via the transport line. The transport line has about 15 m length, covered with metal pipes. Several mirrors are installed in the transport line to change directions of the laser path. In the main optical table, the laser beam is split into two and the split paths

<sup>3</sup> In optics, laser spot size is defined as  $2\sigma$  width of a Gaussian power distribution.

Crossing angle	$w$ [mm]	$f$ [mm]	$w_0$ [ $\mu\text{m}$ ]
$2^\circ$ , $8^\circ$ and $174^\circ$	3.53	250.1	21.0
$30^\circ$	3.53	300.1	25.2
laser wire	10.58	250.0	7.0

Table 2

Planned laser spot sizes at the IP.  $w$ ,  $f$  and  $w_0$  stand for spot sizes at the focal lenses, focal lengths of the lenses, and spot sizes at the IP, respectively.  $M^2 = 1.75$  (measured value) is used to calculate spot sizes.

are intersected at the IP. To obtain a wide observable  $\sigma_y^*$  range from 25 nm to 6  $\mu\text{m}$ , the crossing angle of the split laser paths can be mechanically switched among  $2^\circ$ ,  $8^\circ$ ,  $30^\circ$  and  $174^\circ$  (See Fig. 2). The laser beams are focused at the IP to achieve high photon density. Calculated average number of Compton photons is about 4400/bunch, using 21  $\mu\text{m}$  design laser spot size (except for the  $30^\circ$  mode, which has 25.2  $\mu\text{m}$  spot size because of geometrical restrictions) at the IP. For  $\sigma_x^*$  measurement, a laser-wire is used instead of a Shintake monitor. The spot size at the IP is reduced to 7.0  $\mu\text{m}$  ( $2\sigma$ ) to observe 2.8  $\mu\text{m}$   $\sigma_x^*$ .

Figure 6 shows an optical design of the table. The laser beam comes from bottom-left corner(1), and goes through a beam reducer(2), which reduces the laser beam size to a half, 3.5 mm to avoid tail cuts by optical components in the table. A 95% reflection mirror(3) is placed after the beam reducer. Transmittant laser beam (5% energy) goes to a diagnostic section which consists of a laser position monitor(PSD)(4) and a laser profile monitor(5).

Reflected beam (95%) goes to a 50% beamsplitter(6), which divides the laser path to upper and lower. In the upper path just after the beam-splitter, we install a phase scanner system(7). Selection of the operation modes is performed by angle selection mirrors, which are placed in both of laser paths(8). They can select  $2^\circ$ ,  $8^\circ$ ,  $30^\circ$  and  $174^\circ$  crossing angle modes by rotating themselves by stages below the mirrors. In addition, selection of laser-wire mode needs the angle selection mirrors. In the laser-wire mode, lower rotation mirror is set as same as  $174^\circ$  setup, and upper mirror is set to send the laser path to the absorber. The laser beams are focused by final focusing lenses(9). For the laser-wire mode, a  $3\times$  beam expander(10) is inserted at the laser path to obtain smaller spot size at the IP. Planned laser spot sizes for these crossing angles are shown in Table 2.

The right half of the table is mainly for diagnostics. A couple of Phase monitors is shown as (11). Each of them consists of an objective lens with an image sensor. Delivered paths of laser beams to the objective lenses are different for each crossing angle. Other monitors in the right side are position sensitive detector (PSD)s(12) and photodiode (PD)s(13) for position feedback, intensity

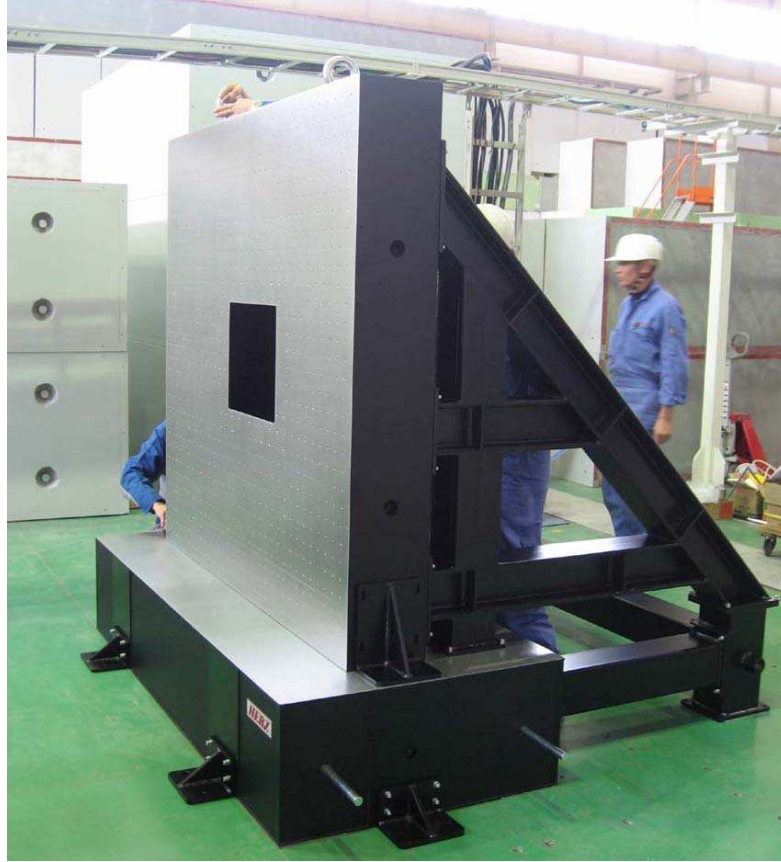


Fig. 7. The main optical table with a support frame. Optical parts and a vacuum chamber will be attached on the vertical plane.

jitter correction and accurate alignment. We implement the optical layout so that a couple of PSDs and PDs can cover all crossing angles. In  $174^\circ$  mode other PSDs and PDs are installed for better stabilization. Image inversion prisms(14) are installed to arrange the image directions of the laser beam at the IP in parallel. This arrangement significantly suppress contrast degradation of the fringe at the IP caused by laser beam position fluctuations.

To suppress the vibration of the table with respect to the electron beam, a rigid support frame is fabricated. Figure 7 shows a picture of the table with the support frame. The main table is made of a 250 mm thickness steel honeycomb core. Total weight is about 2000 kg, including weight of the main table (700 kg). The table is fixed to the ground independent of the final focusing magnets. Since the table of the final focusing magnets is also attached firmly to the ground, both the Shintake monitor and the focusing magnets are expected to move together with the ground. 10 nm level stability of the relative motion between the Shintake monitor and the magnets is targetted.

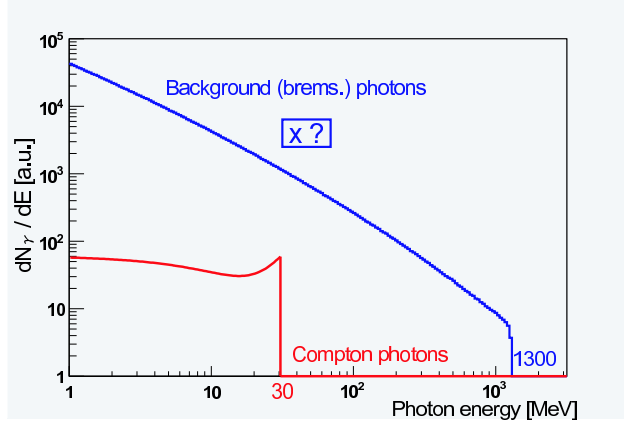


Fig. 8. Energy spectrum of Compton signal and beam background. Since ratio of signal and background is unknown, vertical axis is arbitrary scaled for each spectrum.

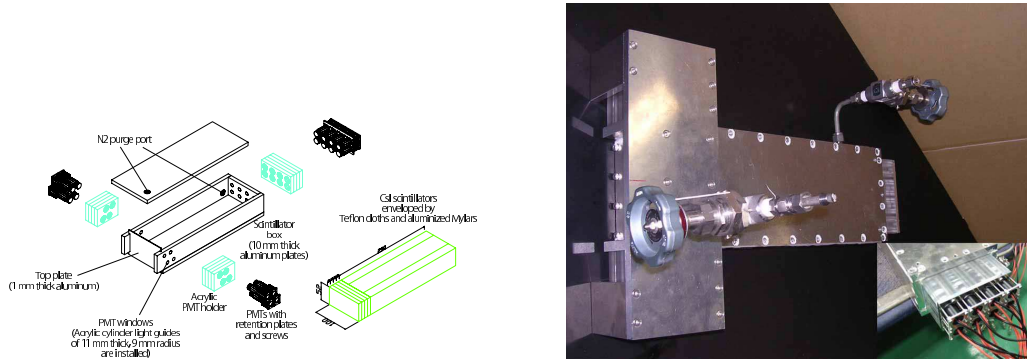


Fig. 9. Components drawings and a picture of the gamma detector.

### 2.3 Gamma Detector

The gamma detector is installed on the beam line after the IP, besides the beam dump. Figure 8 shows energy spectra of Compton photons (signal) and background. Drawn background is from the beam pipe scattering with beam halo electrons. Compton photons have maximum energy of around 30 MeV, and background photons have broader energy range up to 1.3 GeV. Since the amount of background is expected not to be negligible, we need to suppress or subtract the background.

Figure 9 shows a drawing and a picture of the detector. The detector consists of 4-layer forward scintillators and 3 pieces of bulk scintillators. Scintillators are made by thallium-doped cesium iodide (CsI(Tl) : 1.86 cm  $X_0$ ) crystals. Total scintillator size is 100 mm width, 50 mm height, and 330 mm (17.7  $X_0$ ) along the beam axis, enough volume for < 1.3 GeV photons. Each scintillator piece is optically separated by wrappings of a 200  $\mu$ m-thick Teflon sheet and a 50  $\mu$ m-thick aluminized Mylar. The forward scintillators are 10 mm thick (0.54  $X_0$ ) along the beam axis, equipped with photomultiplier tubes (PMT)

on each side. The bulk scintillators have 290 mm ( $15.6 X_0$ ) length, 25 mm (side) or 50 mm (center) width and 50 mm height. Two (side) or four (center) PMTs are attached at the end side of each scintillator. Since CsI(Tl) crystal is slightly hygroscopic, we made a semi-airtight container with sealing by silicon glue and sheet, to close up all the scintillators together. The container is also equipped with a couple of gas inducers, purging by dry nitrogen periodically. The equipped PMTs are Hamamatsu R7400U, which have 8 mm active diameter, operated with positive HV power supply. The PMTs are mechanically attached to the container with support structures. Acrylic cylinder light guides are installed and glued to the container, and PMTs are touched to the light guides. No optical cements are used to enable easy replacement of PMTs. Signals from PMTs are sent to a charge-sensing ADC. The gate of the ADC is planned to be derived from BPM signal, which has almost no jitter.

Detailed description and performance estimation including calibrations and beam tests are described elsewhere[8].

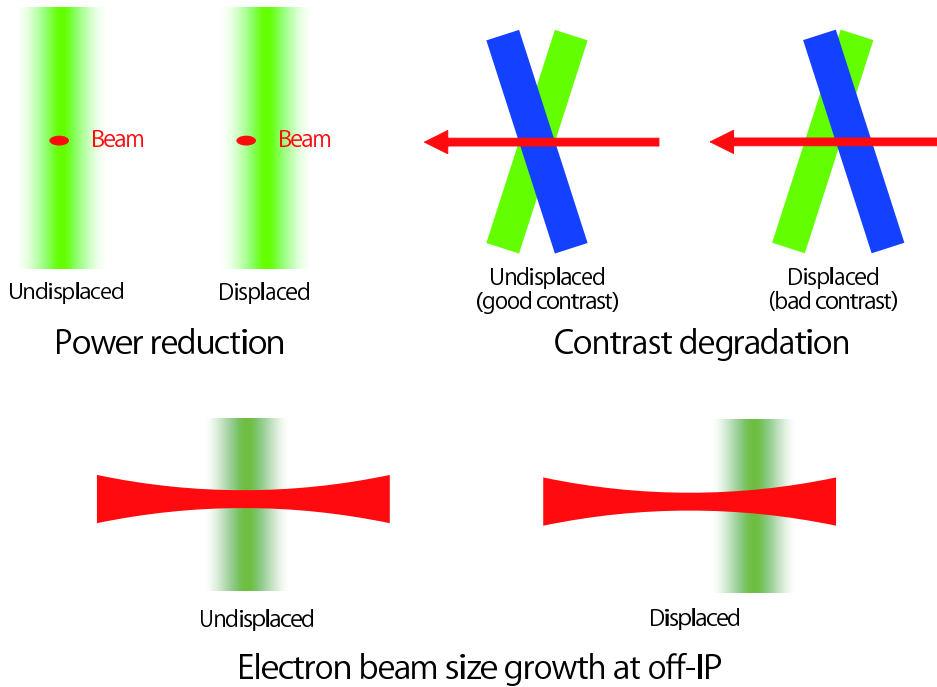


Fig. 10. A schematic view of the three effects by the displaced laser beams.

### 3 Laser Position Alignment and Stabilization

Alignment and position stabilization of the laser spots at the IP are critical issues for the Shintake monitor. Since the laser spot position errors degrade beam size measurements, we need to minimize and/or compensate the position errors.

#### 3.1 Effects of Displaced Laser Beams

Firstly we overview effects of displaced laser beams, caused by misalignment and instability of the laser beam. The effects of the displaced laser beams are categorized into three error factors: power reduction, contrast degradation and electron beam size growth. Figure 10 shows a schematic view of these three effects. Both short-term position instability and long-term position displacement (or misalignment) should be considered to understand these effects.

##### 3.1.1 Power Reduction

A displacement of the laser beam causes a deviation of photon density at the IP. The photon density at the IP with a displacement of laser beam position

on the  $x$ - $y$  plane is described as,

$$P(\delta_x) = P_0 \exp\left(-\frac{\delta_x^2}{2\sigma^2}\right), \quad (2)$$

where  $\delta_x$  is the displacement,  $\sigma$  is the laser spot size, and  $P_0$  is the photon density at no displacement.

For this error factor, we only need to consider the short-term position instability since the long-term position displacement only causes a constant power reduction and then it does not give significant effects to the modulation measurements. However, when average laser spot position is displaced, power fluctuation due to the position fluctuation is enhanced, since the  $P(\delta_x)$  has flat distribution around the  $\delta_x = 0$  and non-flat at the larger  $\delta_x$ . Consequently, we should also care the long-term position displacement if non-negligible position fluctuation is inevitable.

### 3.1.2 Contrast Degradation

Contrast degradation is induced by the relative displacement of two crossing laser beams. The contrast is affected by both short-term and long-term position displacements.

Contrast degradation is caused by power imbalance of the two laser spots, given by[3b],

$$M_\gamma = \frac{(A_1 + A_2)^2 - (A_1^2 + A_2^2)}{A_1^2 + A_2^2} = \frac{2A_1A_2}{A_1^2 + A_2^2} = \frac{2\sqrt{P_1P_2}}{P_1 + P_2} \equiv \frac{2\sqrt{P_A}}{1 + P_A} \quad (3)$$

where  $A_1$  and  $A_2$  are amplitudes of the 2 light paths,  $P_1$  and  $P_2$  are powers of them, which are square roots of  $A_1$  and  $A_2$ .  $P_A$  is defined as  $P_2/P_1$ , which shows the power imbalance.

Response of the spot displacement to the power imbalance is different between displacement along the  $x$ - $y$  plane and along the  $z$  axis.

For the displacement along the  $x$ - $y$  plane, the contrast degradation is given by,

$$M_{\gamma,\delta_x} = \frac{2 \exp\left(-\frac{\delta_{x1}^2}{4\sigma^2}\right)}{1 + \exp\left(-\frac{\delta_{x1}^2}{2\sigma^2}\right)}, \quad (4)$$

where  $\delta_x$  is the displacement and  $\sigma$  is the laser spot size. In this calculation

the electron beam is assumed to pass through the peak of the one of the laser spot (the worst case for the contrast degradation).

For the displacement along the  $z$  axis,

$$M_{\gamma, \delta_z} = \exp\left(-\frac{\delta_z^2}{8\sigma^2}\right). \quad (5)$$

where  $\delta_z$  is the displacement. The contrast is usually much sensitive to displacements along the  $z$  axis than along the  $x$ - $y$  plane.

### 3.1.3 Electron Beam Size Growth at the Off-IP

To achieve extremely small electron beam size at the IP, the electron beam is strongly focused at the IP, with a wide dispersion angle. Because of this wide dispersion angle, waist length of the electron beam around the IP is very short. If the laser spot position fluctuates along the  $z$  axis, the effective beam size is enhanced.

Vertical electron beam size  $\sigma_y$  depends on the position along the electron beam axis( $z$ ) as,

$$\sigma_y(z) = \sqrt{\beta_y^* \epsilon_y \left(1 + \frac{z^2}{\beta_y^{*2}}\right)} = \sigma_y(0) \sqrt{1 + \frac{z^2}{\beta_y^{*2}}} \quad (6)$$

where  $\beta_y^*$  is the beta function at the focal point which is 100  $\mu\text{m}$  in ATF2, and  $\epsilon_y$  is the vertical emittance.

## 3.2 Alignment

In this subsection we discuss about the laser beam position alignment at the IP. Position alignment along the  $x$ - $y$  plane is performed by beam scan and alignment along the  $z$  axis is performed by slit scan.

### 3.2.1 Beam Scan

For an alignment along the  $x$ - $y$  plane, we use the electron beam itself to cross two laser beams just on the electron beam line. Figure 11 shows a schematic of the beam scan. Beam position at the IP can be shifted by an actuator or a stage at the forward mirror, to scan the electron beam. When the laser beam is just at the electron beam position, Compton scattered photons are emitted



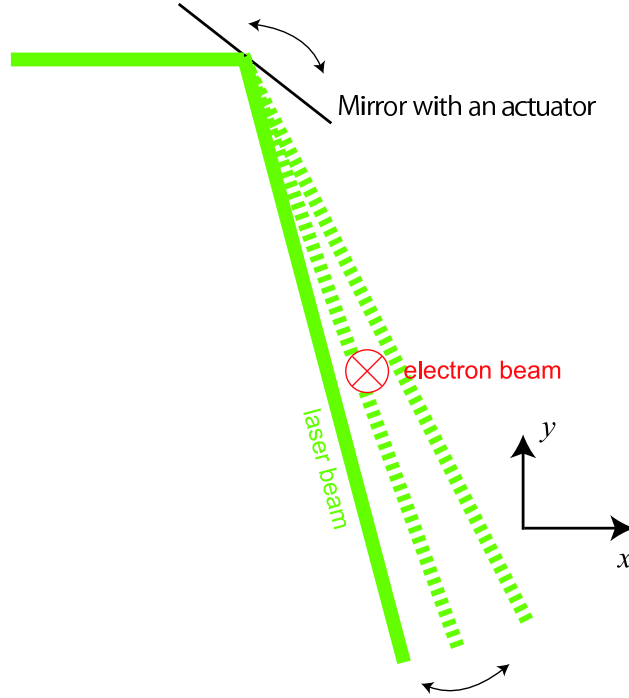


Fig. 11. A schematic of the beam scan along the  $x$ - $y$  plane. The electron beam is scanned by the laser beam with an actuator at the final focus lens. Compton scattered photons are monitored by the gamma detector to obtain the alignment position, which is the position where the maximum number of photons is obtained.

and they can be monitored by the gamma detector of our monitor. We set the alignment position where the Compton signal strength is the maximum.

For the beam scan, only one laser path is introduced to the IP at a time, because we must avoid forming the interference fringe during the beam scan. The other beam path is sent to the absorber by the rotation stage.

We performed a toy Monte Carlo simulation to estimate alignment accuracy of the beam scan. With estimated error factors (4.2% power, 2.5  $\mu\text{m}$  position, and 8.3% background jitter), 0.6  $\mu\text{m}$  alignment accuracy can be obtained[4].

### 3.2.2 Slit Scan

The left figure of Fig. 12 shows a schematic of the alignment along the  $z$  axis called a “slit scan”. A slit made by stainless steel is inserted at the IP. Mirrors equipped with actuators can steer the laser beam across the slit, and photodiodes after the IP monitor the arrived light intensity which passed through the slit. The right figure of Fig. 12 shows the detected photodiode intensity during the slit scan. The slit width is 500  $\mu\text{m}$ , which is much wider than the laser spot size. Obtained graph can be expressed as,

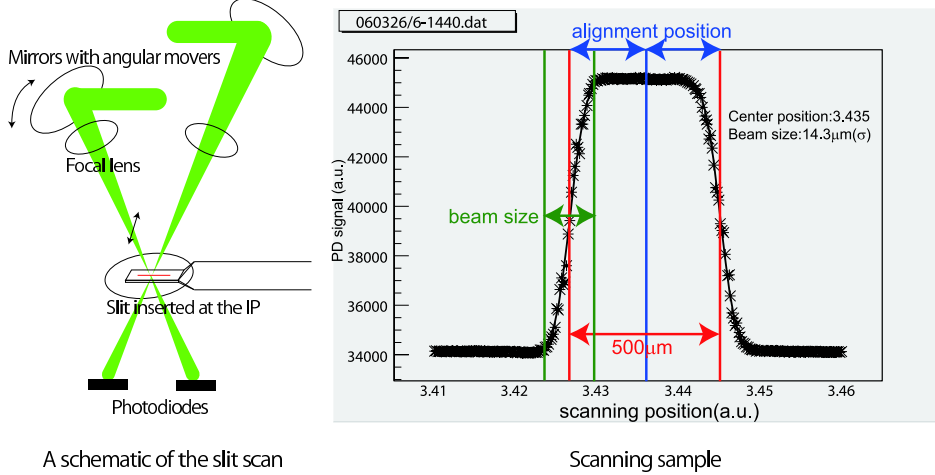


Fig. 12. Sample data of slit scan by low power test laser.

$$P(x) = C \left\{ \operatorname{erf} \left( \frac{x - \mu + w/2}{\sigma} \right) - \operatorname{erf} \left( \frac{x - \mu - w/2}{\sigma} \right) \right\} \quad (7)$$

$$\operatorname{erf}(x) \equiv \frac{1}{\sqrt{2\pi}} \int_0^x e^{-t^2/2} dt \quad (8)$$

where  $x$  is the laser position,  $C$  is amplitude,  $\mu$  is the center position of the slit,  $w$  is the width of the slit, and  $\sigma$  is the laser spot size ( $1\sigma$ ).  $\operatorname{erf}(x)$  is an integral of Gaussian function, called “error function”. The line in Fig. 12 shows the fitting result by  $P(x)$ . We can adopt fitted  $\mu$  for the alignment target.

Positions of the laser spots are monitored by PSDs. Accuracy of the alignment is limited by linearity of the PSDs, which is  $< 9.1 \mu\text{m}$  (measured value). Position uncertainty caused by this linearity is  $< 1.7 \mu\text{m}$  by optics calculations.

To align the electron beam waist to the center of the laser spots, electron beam waist position is adjusted by controlling strength of magnetic field of the final quadrupole. Required position accuracy of the beam waist is about  $20 \mu\text{m}$ , which is achievable by this method.

Slit scan is also used for the laser spot size measurement at the IP. The spot size is obtained by fitting data around the edge of the slit by an error function (8). The measurement is fluctuated by the laser power jitter and the position jitter. We performed a toy Monte-Carlo simulation with estimated error factors (1% laser power,  $2.5 \mu\text{m}$  position jitter), and obtained that accuracy of spot sizes is  $0.9 \mu\text{m}$ .

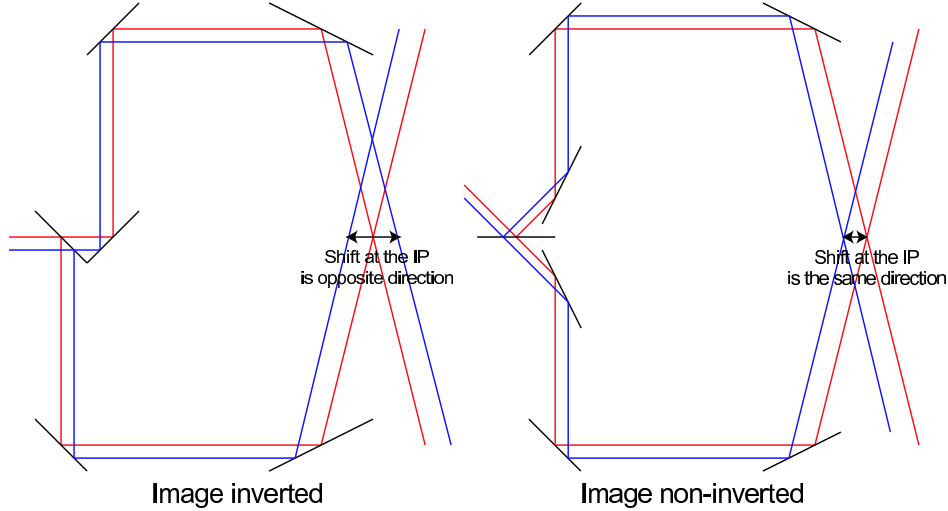


Fig. 13. A schematic of the image inversion. If the beam line is image inverted (Left figure), the position displacement at the laser or forward optics causes displacements of the opposite direction at the IP. If the beam line is non-inverted (Right figure), it causes displacements of the same direction at the IP.

### 3.3 Stabilization and Correction

As transient position displacements of the laser spots, angular jitter of the laser and slow drift (by temperature etc.) should be considered.

#### 3.3.1 Correction of the Laser Angular Jitter

An intrinsic angular jitter of the pulsed laser is the largest source which causes pulse-to-pulse laser position fluctuations. Measured value of the angular jitter is about  $10 \mu\text{rad.}$ , while it may vary by environmental conditions. This jitter cannot be actively stabilized, but it can be monitored by PSDs. Since the position displacement caused by the angular jitter is enhanced by the long transport line, the jitter can be monitored precisely by PSDs. Using the measured RMS pulse-to-pulse resolution of our PSDs  $9.1 \mu\text{m}$ ,  $1.0 \mu\text{rad.}$  resolution is achievable.

The measured angular jitter is used to correct the power fluctuation caused by the angular jitter. In case of  $10 \mu\text{rad.}$  angular jitter, the power fluctuation is 3.9% without correction. It can be corrected within 1.4% accuracy using the measured angular jitter (toy Monte-Carlo estimation again).  $0.6 \mu\text{m}$  alignment accuracy along the  $x$ - $y$  plane (see Section 3.2.1) is used for the estimation.

For the contrast degradation, selecting proper “image direction” enables to cancel the displacement between the two laser paths. Figure 13 shows a schematic of the image inversion. The blue and red laser beams are positionally displaced,

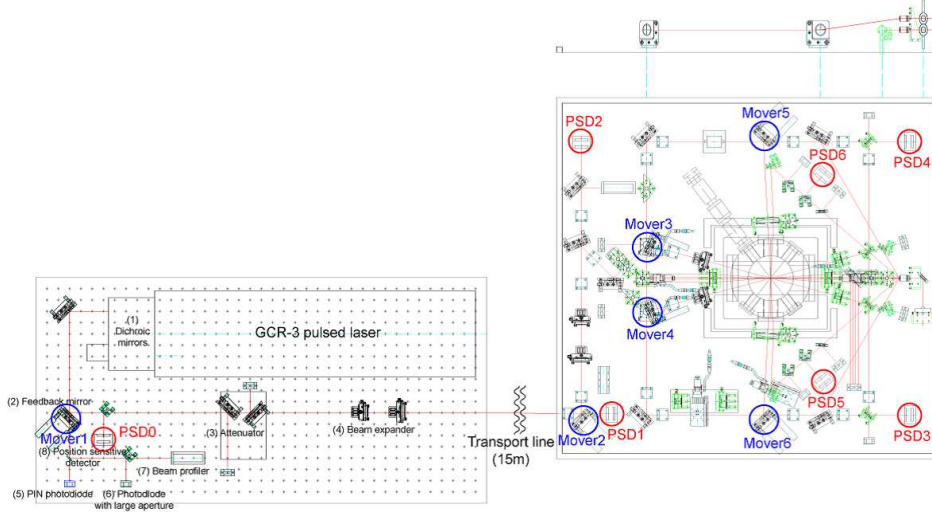


Fig. 14. Position of the actuators and the position sensitive detectors.

which causes the position deviation at the IP. In the image-inverted (left) figure, the direction of the displacement at the IP is the opposite direction to each other, while in the image non-inverted (right) figure, the direction is the same.

The figure shows the case of position displacement, but the response of the angular jitter is the same as the position displacement. To suppress the contrast degradation by the laser angular jitter, the image direction is designed to be the same for the incoming beam lines in our optical table, using Dove prisms to flip the image direction.

With the proper image direction, contrast degradation caused by the angular jitter can be suppressed to negligible level.

For the off-IP beam size growth, the position jitter is negligible, because  $20\ \mu\text{m}$  position displacement (1 order of magnitude larger than the displacement caused by measured angular jitter) only causes 2% beam size growth.

### 3.3.2 Stabilization of Slow Drift

The slow laser beam position drift (timescale larger than minute) can be induced by plenty of error sources, laser drift, physical shift of the laser transport line, angular shift of the optical components on the optical table, etc. Since the measurement time of the Shintake monitor is 1 minute, the slow drift causes only an alignment error. It can be canceled by active stabilization using USDs and mirror actuators.

The installed location of the PSDs are shown in Fig. 14. A geometrical laser path (which is a drift space without any mirrors or lenses) is defined by 4

variables, center position (x,y) on a certain plane and forward angle (azimuth and elevation). To stabilize a laser path, we need 2 PSDs and 2 actuators for both position and angle.

The drift from the origin of the laser and the transport line (outside-origin drift) has larger amplitude than the drift from the origin on the optical table (inside-origin) because laser has a lot of instability and the environmental condition is worse for the transport line. The outside-origin drift is canceled by locally PSD1 and PSD2 with Mover1 and Mover2, to prevent the outside-origin drift from affecting the optics on the table. PSD 3 - 6 with Mover 3 - 6 are mainly for the alignment, but the inside-origin drift can also be canceled using these PSDs and movers.

Because of the large angular jitter of the laser, we need to average  $\sim 100$  pulses for the active stabilization with high accuracy (better than alignment accuracy). Therefore, stabilization of  $< 1$  minute is not feasible. We expect that the drift within the measurement time is smaller than the alignment accuracy.

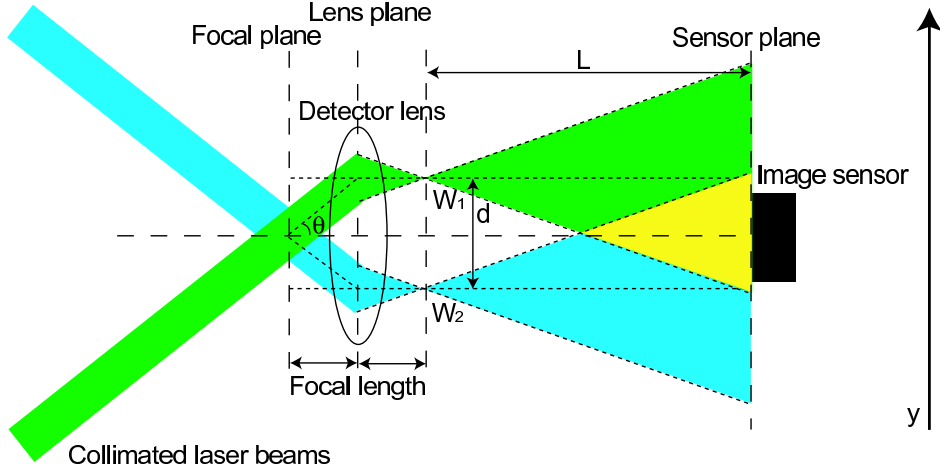


Fig. 15. Schematic of fringe magnification by a lens. Approximation of geometrical optics is applied in this figure.

## 4 Phase Control

Fluctuations of the relative phase of the two laser beams at the IP cause fluctuations of the fringe pattern. To suppress the phase fluctuation, an active phase control system is implemented in our Shintake monitor. In addition, phase scanning to obtain modulation spectrum is also performed using the phase control system. The phase control system consists of phase monitors and a phase mover with a active feedback software.

### 4.1 Phase Monitor

A schematic drawing of a phase monitor is shown in Fig. 15. The phase monitor consists of a lens for fringe magnification and an image sensor for fringe pattern acquisition.

Split laser beams are collimated and introduced to the detector lens as the center of the laser beam goes through just the focal point of the lens. Since light from the focal point goes parallel to the lens axis after passing through the lens, the center of the laser beam goes along the lens axis. Surrounding light of the laser beam is focused on the opposite focal plane and then diverged as shown. Interference fringe is formed in the overlapped area (painted yellow). Obtained fringe phase at the image sensor corresponds to a phase difference of the two laser beams at the focal plane.

To accept large crossing angles, focusing power of the detector lens must be very large. We use an objective lens whose focal length is 2 mm ( $100\times$  multiplication), NA (numerical aperture) = 0.95. Crossing angles up to  $144^\circ$  can be

monitored via the objective lens. With the objective lens, we can obtain clear interference fringes, which can be observed by the image sensors.

A CMOS linear image sensor is used for the phase acquisition. It has 1024 pixels in  $7.8 \mu\text{m}$  pixel pitch, and its readout frequency is 187 kHz / pixel. The pixel data are sent to a 200 kHz 12 bit VME ADC. Data from two image sensors can be read interleaved in 10 Hz repetition rate (corresponding to every laser pulse).

To extract phase information from the waveform data, we use Fourier transformation method. Fourier transform is defined as,

$$g(\omega) = \int_{-\infty}^{+\infty} f(t)e^{-i\omega t} dt \quad (9)$$

where  $f(t)$  is an original function and  $\omega$  is an angular velocity, which is the base of the transformation. Physically,  $|g(\omega)|$  represents fraction of power at the angular velocity of  $\omega$ , and  $\arg g(\omega) = \tan^{-1} (\text{Im } g(\omega)/\text{Re } g(\omega))$  represents phase at  $\omega$ .

A fringe pattern makes a sine curve at the image sensor. A sine function is converted to a delta function which has a peak at the sine frequency by Fourier transform. We can get the phase of the sine function by calculating  $\arg g(\omega)$  at the delta-peak frequency.

Fourier transform assumes that  $f(t)$  is perfectly smooth from  $-\infty$  to  $+\infty$ , while in fact the waveform is discrete and restricted in a finite region. In real analysis, we modify the transform as

$$g(j) = \sum_{k=-N/2}^{N/2-1} f_k \exp\left(-\frac{2\pi i j k}{N}\right) \quad (0 < j < N). \quad (10)$$

where  $f_k$  is a point of discrete waveform.

This modification is slightly different from ordinal Discrete Fourier Transform (DFT). First, the ordinal DFT calculates only integer  $j$ , though fractional  $j$  is also used for our analysis to obtain better resolution of the peak frequency. Second, summing range of  $k$  is shifted to  $(-N/2, N/2 - 1)$ , compared to the ordinal DFT  $(0, N - 1)$ . This modification suppresses a phase jitter caused by a position error of the peak frequency.

Figure 16 shows sample waveforms of a phase acquisition. In Plot (A) (raw waveform), a clear fringe pattern is observed. Plot (B) shows a Fourier power spectrum. The fringe pattern in Plot (A) corresponds to the peak around

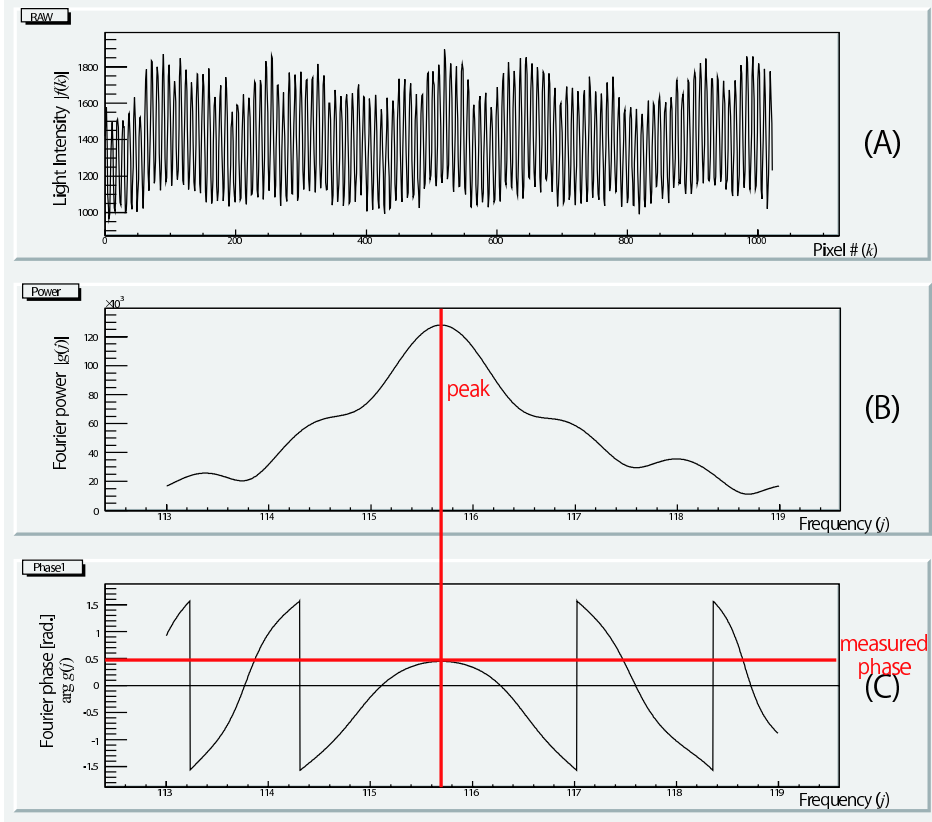


Fig. 16. A detection sample of Fourier transform. (A): a raw waveform captured by the image sensor. (B): Fourier power spectrum  $|g(j)|$  around the peak. We can observe a peak of power spectrum at  $f \sim 116$ . (C): the phase spectrum,  $\arg g(j)$  of (10). The red line shows the peak position of the Fourier power spectrum.

$j = 115.7$  in Plot (B) (zoomed around the peak). Plot (C) is a Fourier phase spectrum. Measured phase in this sample is shown as the horizontal line of the plot, phase value at the peak of the power spectrum. This measured phase is used for reference data of the phase control.

## 4.2 Phase Control

To adjust and sweep the fringe phase, we install a phase mover on one of the split laser paths. It consists of a piezoelectric stage and prisms to form an optical delay line of variable length. The fringe phase at the IP depends on the difference of the two split laser path length, then the phase can be controlled by adjusting one of the path length using the stage.

Figure 17 shows a schematic of the optical delay line. The laser path is reflected at the orthogonal planes of the bottom prism (with high reflection coatings), and folded by the top prism (total internal reflections). The top prism is on a piezoelectric stage, which has 0.2 nm closed-loop resolution. The path length



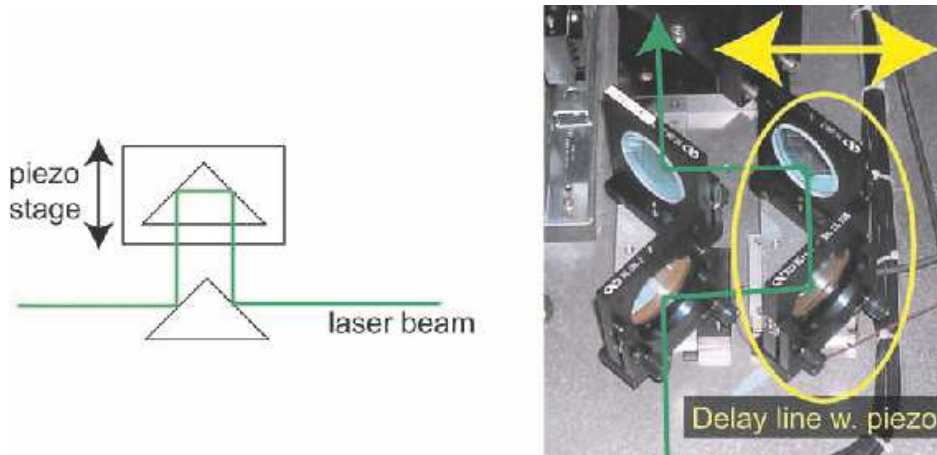


Fig. 17. A schematic figure of the variable optical delay line (left) and a picture of its test setup (right). The test setup uses mirrors instead of prisms.

can be tuned using the stage at 0.4 nm resolution. Response time of the stage is fast enough for  $< 10$  Hz phase control system.

The stage accepts a position input by an analog voltage. The position input signal is controlled by a VME 16 bit D/A board with a phase control software. In the phase control software, the image sensor is triggered soon after laser pulse, and the fringe waveform is acquired via VME ADC board. Phase calculation is performed using the waveform by Fourier analysis. After the calculation, the position input signal is set to cancel the deviation of the monitored phase to the target value.

### 4.3 Monitoring Location

For the Shintake monitor, we need to stabilize the fringe phase at the IP. Since we cannot install the phase monitor at the IP, we have to install the monitor at other locations. When we control the fringe phase viewed at the monitor location, the phase difference between the IP and the monitor location causes a phase error at the IP.

To minimize the error, two phase monitors are installed in  $174^\circ$  crossing angle mode. As shown in Fig. 18, one of the monitors, which is located at 150 mm height from the table surface, views the relative phase of the laser beams separated from the main laser beam lines before the IP (green line), and the other monitor, located at 100 mm height, views the laser beams which have passed through the IP (red line). Since the IP is between the two monitoring position, the phase at the IP is considered to be between measured phases by the two monitor. The two monitors are used to improve the phase accuracy at the IP and to estimate the effectiveness of the phase stabilization at the IP.

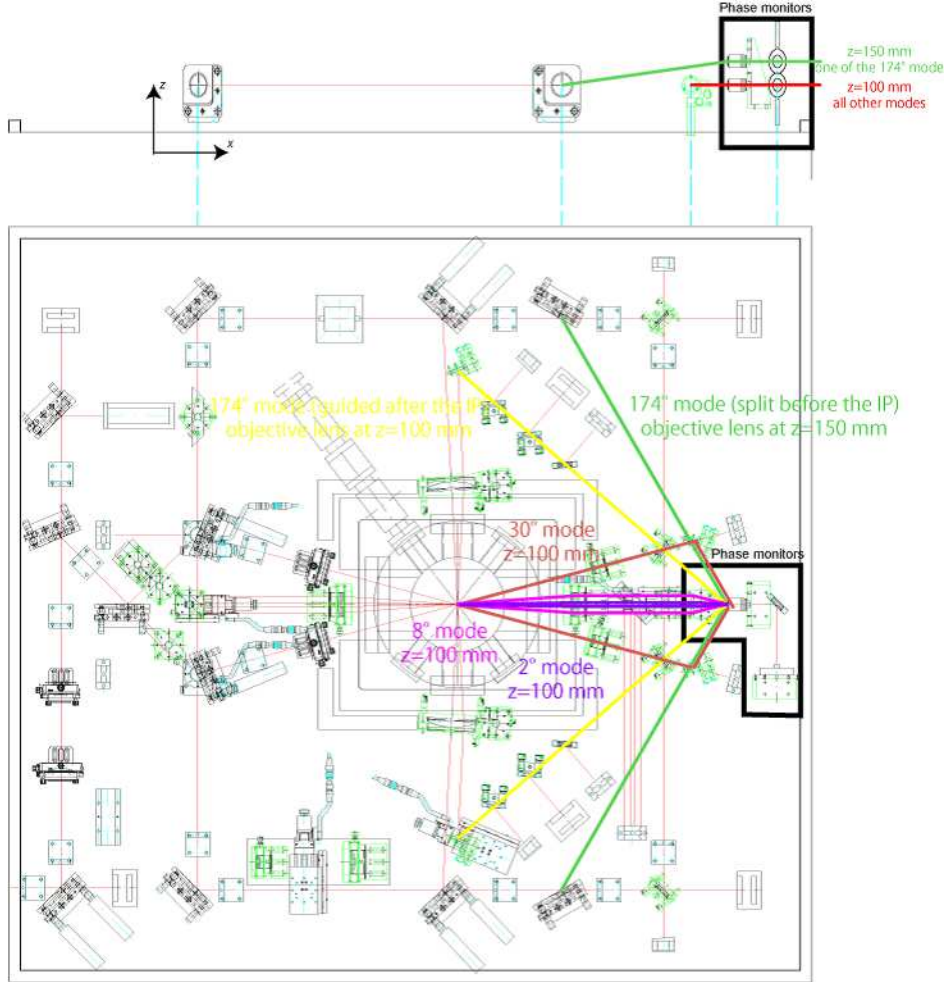


Fig. 18. Locations and laser paths of the phase monitors. The phase monitors are installed at  $z = 100$  mm and  $150$  mm. The  $150$  mm monitor is only used for the  $174^\circ$  mode optical path split before the IP. The  $100$  mm monitor accepts the  $174^\circ$  mode path guided after the IP, and paths from all lower angle modes.

For other angle modes, only one phase monitor is active because of geometrical restrictions. Since the accuracy is less important in these angle modes, it is not seriously concerned if the phase accuracy is not assured.

#### 4.4 Tests of Phase Monitoring and Stabilization

##### 4.4.1 Measurement Condition

To obtain a performance of the phase monitoring and the stabilization, we did test experiments of the phase monitoring and the control. For the phase control test, a couple of objective lenses with image sensors, and a delay line with a piezo stage, as all described in former sections, are used. We split the laser beams and form two beam crossings to be viewed by the phase monitors

(Ch1 and Ch2), as same as  $174^\circ$  setup of the real Shintake monitor. The two monitors are used to estimate the performance of the phase stabilization.

To estimate the performance of the phase stabilization for the Shintake monitor, the following method is applied.

- Obtain and record phase data from both monitors.
- Feedback routine calculates the motion of the phase mover to stabilize the Ch1 phase. Ch2 phase is recorded but not used for the stabilization.
- Analyze the phase stability of Ch2 phase. The Ch2 phase stability indicates the stability at the IP of the Shintake monitor for the real setup.

Figure 19 shows the setup of the experiment. The experiment is performed on the existing optical table used in the FFTB Shintake monitor with additional instruments. The stabilization measurement is performed using the pulsed laser to be used in the real ATF2 Shintake monitor, and a low power continuous wave (CW) laser for a comparison.

#### 4.4.2 Result of the CW Laser Test

Figure 20 (A) shows a typical result of the phase monitoring without the phase stabilization. Because the phase monitors are located face-to-face, phase variation can be observed inversely to the other. The anti-correlation of two monitors can be seen by adding two data (the blue line). It shows a strong anti-correlation on the 10 minutes window in the figure. The anti-correlation factor is expected to be the relative phase fluctuation between the incident two laser beams. The data of individual channels show a fluctuation of relatively short period of  $\lesssim 1$  minute and a long term drift over the 10 minutes window.

Figure 20 (B) shows a typical result of the phase monitoring with the phase stabilization. Ch1 is stabilized to phase = 0, which results in a very flat plot of the red line. Ch2 is not stabilized, but because the stabilization is performed before splitting the laser path, Ch2 is also affected by the stabilization. The phase variation of Ch2 is drastically suppressed compared to the unstabilized data, while the pulse-to-pulse fluctuation seems to increase slightly due to the phase stabilization.

For our modulation measurement, stability in 1 minute (time for single measurement) is concerned. To obtain 1 minute stability, we sliced the phase data to 1 minute windows and acquire RMS values in the window.

The averages of the Ch2 RMS phase fluctuations in 1 minute windows are 27.5 mrad. with stabilization of Ch1 (corresponding to the green line in Fig. 20 (B)), and 73.6 mrad. without stabilization (the green line in Fig. 20 (A)). A clear effect of phase stabilization is observed.

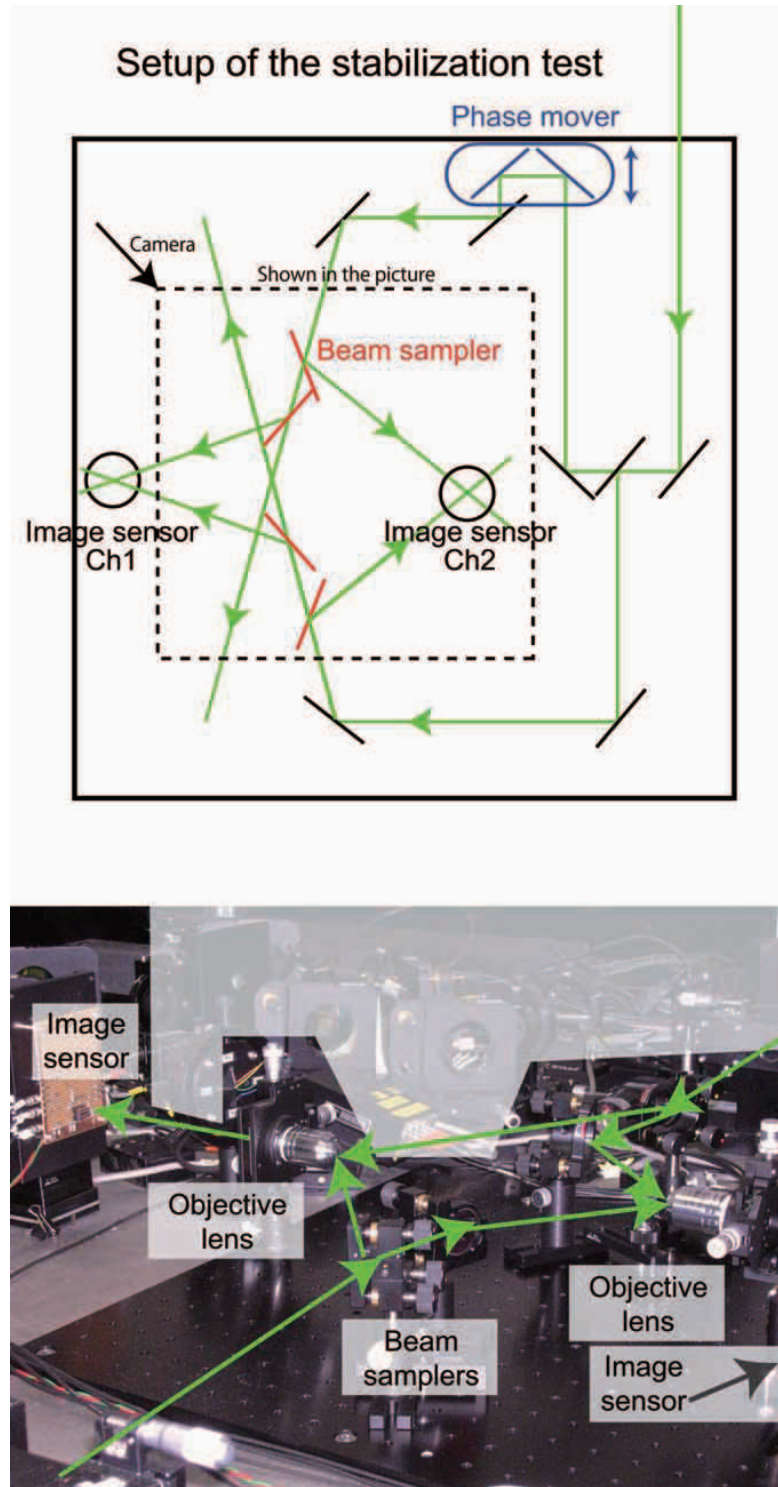


Fig. 19. Upper: the layout of the stabilization test. Lower: a picture of the test setup of the phase monitoring.

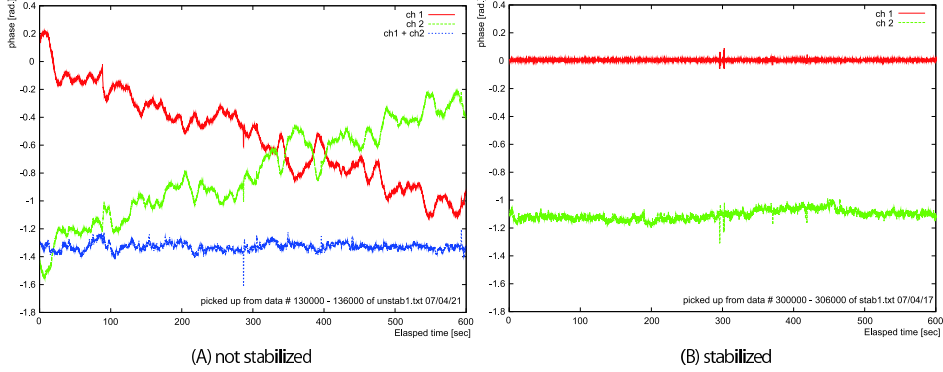


Fig. 20. A sample result of the phase monitoring in a 10 minutes window (A) without phase stabilization and (B) with phase stabilization. In (A), an addition of both channels is shown in the blue line.

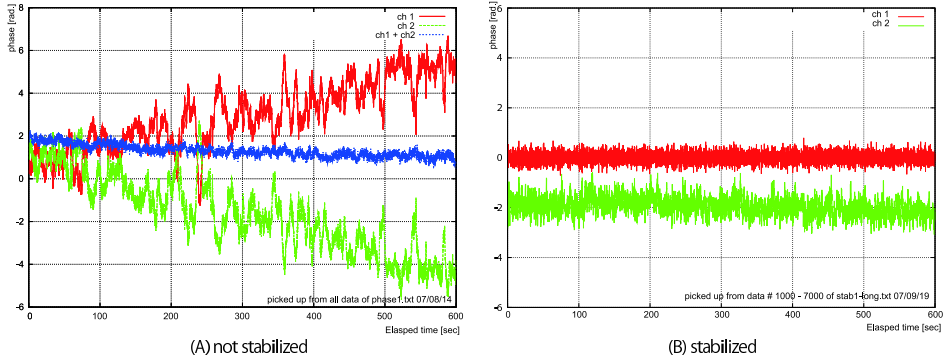


Fig. 21. A sample result of the phase monitoring in a 10 minutes window (A) without phase stabilization and (B) with phase stabilization in the pulsed laser. The vertical axis is enhanced compared to Fig. 20.

#### 4.4.3 Result of the Pulsed Laser Test

For the pulsed laser, we perform the same measurement as the CW laser.

Figure 21 (A) shows a typical result of the phase monitoring for the pulsed laser. A pulse-to-pulse fluctuation of around 0.5 radian amplitude can be clearly observed, in addition to the fluctuation of multi-second timescale which can be seen also in the CW laser. The pulse-to-pulse fluctuation can also be observed in the spectrum of adding two channels (blue). Because the fluctuation is pulse-to-pulse and correlation between channels is poor, this fluctuation cannot be canceled nor corrected by the phase monitoring and stabilization system. The RMS phase of the addition spectrum is 170 mrad., which is the limit of the phase stabilization performance for the pulsed laser. For the long term fluctuation two channels are almost correlated and canceled by adding the two channels.

Figure 21 (B) shows a 10 minutes spectrum of a stabilized phase data of the pulsed laser. The stabilization is effective for long term fluctuations, but the

pulse-to-pulse fluctuation is totally remained or slightly enhanced.

The obtained RMS stabilities of 1 minute windows for the pulsed laser are 239 mrad. with stabilization of Ch1 and 800 mrad. without stabilization. Although the stability is quite worse than the stability in the CW laser, it is still in an acceptable range for the target performance of the Shintake monitor. The stability is limited by the pulse-to-pulse fluctuation. The pulse-to-pulse fluctuation seems to be partly caused by the angular jitter, while further study is needed to understand and suppress the pulse-to-pulse fluctuation.

#### *4.5 Beam Position Stability and an IP-BPM*

Electron beam position jitter with respect to the optical table is also a source of the phase jitter. To monitor the electron beam position jitter, a ultra-high precision cavity beam position monitor (IP-BPM) is attached to the optical table of the Shintake monitor. The vertical position resolution of the IP-BPM is demonstrated in ATF and 8.7 nm resolution is already obtained. Performance study of the IP-BPM is described elsewhere[9a–b].

Design beam position stability at the IP in ATF2 is  $1/3\sigma_y$ , about 12 nm for 37 nm beam size. Although the actual position stability is unknown, we can correct the electron beam position using the IP-BPM with 8.7 nm resolution.

#### *4.6 Summary*

In summary, current obtained phase accuracy is about 240 mrad. (corresponding to 10.1 nm) by phase stabilization, and 8.7 nm by IP-BPM. Combining these, 13.3 nm (0.31 radian) is the current estimated phase stability obtained in the real Shintake monitor. For the performance estimation, this 13.3 nm is used for the phase uncertainty in the beam size measurement. This value may be lowered by suppressing pulse-to-pulse fluctuation at the phase monitor, by improving air-flow prevention, and/or suppressing noise of the IP-BPM.

## 5 Fringe Contrast

Contrast of the interference fringe strongly affects modulation measurements. We need to ensure the fringe contrast is perfect, or to know the contrast precisely if it is not perfect. In this section we briefly overview contrast degradation sources, and discuss about the contrast estimation.

### 5.1 Sources of Contrast Degradation

- Power Imbalance

Power imbalance of the crossing two laser beams causes the contrast degradation.

The modification of the modulation depth  $M$  by the power imbalance  $P_I = P_1/P_2$  is given by

$$M' = \frac{2\sqrt{P_I}}{1 + P_I} M. \quad (11)$$

In our design, the power imbalance is estimated to be  $< 12\%$ . Since the calculated modulation degradation by (11) of the  $12\%$  power imbalance ( $P_I = 0.88$ ) is only  $0.2\%$ , the effect of power imbalance can be ignored.

- Position Displacement

Position displacement causes a localized power imbalance and then degrade the fringe contrast. If our design of the position adjustment and the image inversion feature (discussed in Section 3) are correctly worked, the position displacement between two laser beams should be  $< 1 \mu\text{m}$ . Using (11), the contrast degradation is estimated to be  $< 0.3\%$ .

- Imperfect Polarization

Since photons of different polarizations are not interfered, imperfect polarization of the laser photons cause the modulation degradation.

We can estimate the modulation degradation by the limited polarization ratio  $P (< 1)$  as

$$M' = \{P^2 + (1 - P)^2\} M. \quad (12)$$

The polarization factor of our laser is measured to be  $> 99.3\%$ . It corresponds to  $< 0.5\%$  modulation degradation.

- Spherical Wavefront

The focusing laser beams have spherical wavefronts. Wavefront radius  $R$  is determined by Gaussian beam optics as

$$R = z \left\{ 1 + \left( \frac{\pi w_0^2}{\lambda z} \right)^2 \right\} \quad (13)$$

where  $z$  is distance along the beam line from the waist point,  $w_0$  is the waist beam size and  $\lambda$  is the laser wavelength. If the electron beam crosses just on the focal point of the laser beam ( $z = 0$ ), the  $R$  comes infinite and the wavefront is perfectly planar, which can make planar interference fringes. Practically, the electron beam goes through somewhat distant position from the focal point, and the  $R$  comes finite value, which stands for the imperfect planar interference fringes and consequently it results modulation degradation.

The modulation degradation is given by

$$\frac{M'}{M} = \int_{-\infty}^{+\infty} \exp\left(\frac{\rho^2}{w_z^2}\right) \sin\left(\frac{k\rho^2}{2R} - \phi\right) d\rho \quad (14)$$

where  $\rho$  is the position perpendicular to the beam axis ( $\rho = 0$  as beam center),  $w_z$  is the beam size at  $z$ , and  $\phi$  is the phase determined to make the integral maximum.

We assume that the accuracy of the focal length alignment can be achieved to be  $< 400 \mu\text{m}$ , which causes 0.6% contrast degradation.

- Spatial Coherence

If the spatial coherence of the laser beams is poor, the formed interference fringes are distorted at the laser beam tail, and the contrast is degraded.

The spacial coherence become poor if the mirrors or lenses are distorted, especially those in laser paths after the main beamsplitter. We use optical components which have  $1/10\lambda$  or better quality to suppress the coherence degradation. In addition, overlapping of higher-order paths, eg. by back reflection of mirrors, may degrade the spatial coherence, but the effect is suppressed around the focal point because the higher-order paths usually have different focal points.

Though the spatial coherence is difficult to be directly measured, we expect that it is good enough not to degrade the fringe contrast.

- Temporal Coherence

Temporal coherence (also known as coherent length) is one of the basic characteristics of the laser. The laser light outside the coherent length is neither coherent nor interfered. The temporal coherence is determined by the wavelength width of the laser oscillation. Using the laser specifications of the spectral width  $\delta k < 0.003 \text{ cm}^{-1}$  and the difference of the split path lengths of the Shintake monitor  $\Delta L < 100 \text{ mm}$ , the maximum phase variation is

$$\delta\phi = \delta k \Delta L = 3 \times 10^{-2} \text{ [rad.]} \quad (15)$$

which results in  $< 0.6\%$  contrast degradation.

All above contrast degradation effects but the spatial coherence are shown to affect the contrast less than 1% level. We expect that the overall contrast degradation at the IP is less than 10%. Practically we need to measure the



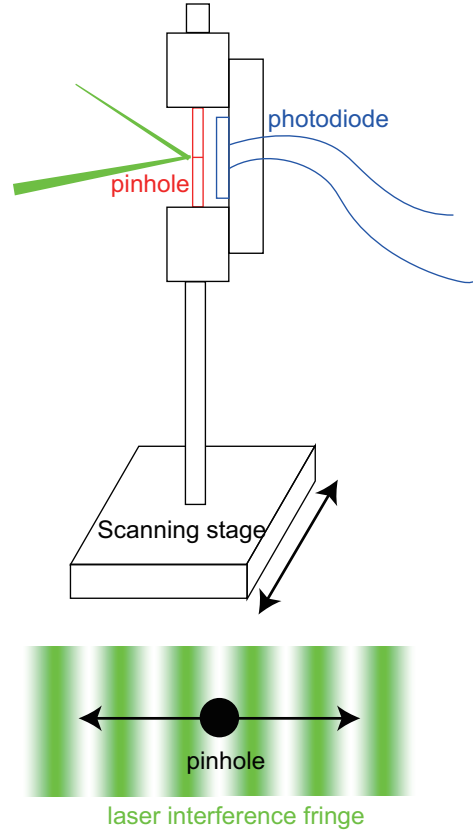


Fig. 22. A schematic of a pinhole fringe monitor. Laser light passing through the pinhole is captured by a photodiode. A motorized stage is equipped to sweep the pinhole across interference fringes.

fringe contrast in the real setup and correct the beam size calculation using the contrast value.

## 5.2 Contrast Measurement

Contrast of the interference fringe is measured using pinholes in a test setup. Figure 22 shows a schematic drawing of the pinhole monitor. In the monitor, a pinhole is placed close to a photodiode, attached to a stage with a motorized actuator. Split laser beams cross at the surface of the pinhole to make interference fringe pattern.

We measure interference fringes formed by both CW and pulsed lasers using this pinhole monitor. For the CW laser,  $1\ \mu\text{m}$  aperture pinhole was used with the crossing angle of  $6^\circ$ . For the pulsed laser,  $1\ \mu\text{m}$  pinhole cannot be used because of heat destruction, thus high-power durable  $5\ \mu\text{m}$  pinhole was used instead with  $2^\circ$  crossing angle. Additional contrast degradation in the measurement due to the finite pinhole diameter was compensated by calculations using

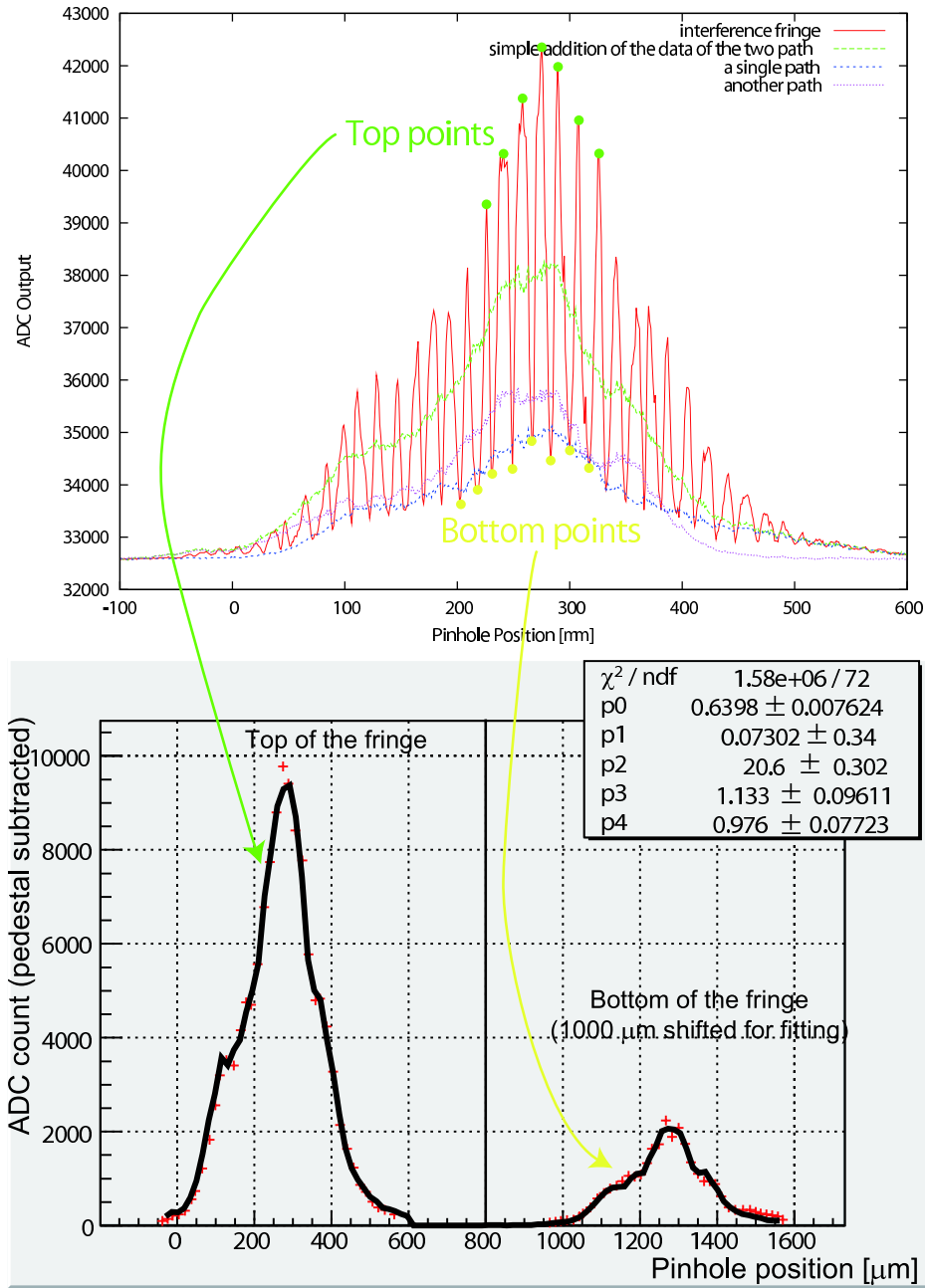


Fig. 23. A contrast measurement of the pulsed laser. Upper: Observed fringe pattern by intersecting two laser paths. The red and blue lines show the intensity of individual paths. Lower: A result of contrast calculation. The top and bottom points are picked up from the fringe pattern, and simultaneously fitted by shifting the bottom points 1000  $\mu\text{m}$ . The fitting function is described in the text. Free parameters of the fitting are: fringe contrast (p0), position shift of each path (p1 and p2), and power shift of each path (p3 and p4).

the pinhole diameters. Relatively large uncertainty of the pinhole diameter (in specification) was treated as a systematic error.

Laser	Angle	Pinhole Aperture	Contrast (raw)	Contrast (compensated)
CW	6°	1.0 <sup>+0.4</sup> <sub>-0.0</sub> μm	70 ± 2.0%	75 ± 2.0(fit) ± 2.5(aperture)
Pulsed	2°	5.0 ± 0.75 μm	64 ± 0.8%	75 ± 0.8(fit) ± 4.0(aperture)

Table 3

Summary of the contrast measurements by pinholes.

Figure 23 shows the result of the measurement with the pulsed laser. To obtain the fringe contrast, following method is used.

- (1) The fringe pattern is formed by intersecting two laser paths. We define the obtained fringe pattern as  $f_{\text{orig}}(x)$ . The pinhole sweeping is also performed for each laser path open and another closed. The obtained distributions are denoted as  $f_1(x)$  and  $f_2(x)$ .
- (2) The peak and bottom points are extracted from  $f_{\text{orig}}(x)$ . The group of the top points are denoted as  $f_{\text{max}}(x)$ , and the group of the bottom points are denoted as  $f_{\text{min}}(x)$ .
- (3) A distribution for the fitting  $f(x)$  is defined as,

$$f(x) \equiv \begin{cases} f_{\text{max}}(x) & (x < x_t) \\ f_{\text{min}}(x - x_0) & (x \geq x_t) \end{cases} \quad (16)$$

In Fig. 23,  $x_0 = 1000$  [μm] and  $x_t = 800$  [μm].

- (4) Using fitting parameters  $p_0 - p_4$ , the fitting function  $g(x)$  is defined by,

$$g(x) = \begin{cases} p_0 \left( \sqrt{p_3 f_1(x - p_1)} + \sqrt{p_4 f_2(x - p_2)} \right)^2 \\ \quad + (1 - p_0)(p_3 f_1(x - p_1) + p_4 f_2(x - p_2)) & (x < x_t) \\ p_0 \left( \sqrt{p_3 f_1(x - p_1 - x_0)} - \sqrt{p_4 f_2(x - p_2 - x_0)} \right)^2 \\ \quad + (1 - p_0)(p_3 f_1(x - p_1 - x_0) + p_4 f_2(x - p_2 - x_0)) & (x \geq x_t) \end{cases} \quad (17)$$

The points of the functions where no data points are provided are defined by interpolations or extrapolations of the nearest two points.  $p_0$  means the fringe contrast (0-1),  $p_1$  and  $p_2$  means the horizontal shifts of the  $f_1(x)$  and  $f_2(x)$ ,  $p_3$  and  $p_4$  means the power fluctuation of the  $f_1(x)$  and  $f_2(x)$ . The initial values of  $p_1$  and  $p_2$  are manually given since the optimization of them is not efficient by the fitting. For the CW laser measurement,  $p_1$  is set to 0.005 [mm] and  $p_2$  is set to 0. The movable range of  $p_3$  and  $p_4$  is limited to  $1 \pm 0.05$ .

- (5) Using  $p_0$  as “the fitted fringe contrast”. From Fig. 23,  $64.0 \pm 0.8\%$  contrast is obtained by the fitting.

Table 3 shows a summary of the contrast measurements. Both lasers give consistent results, and they show that contrast around 75% can be achievable.

Compared to the estimation described in Section 5.1, however, unexpected contrast degradation is measured and the reason is currently unknown. Since contrast in the real setup may be differ from the test setup. We can more reliable contrast measurements using electron beam in the real setup

### 5.3 Contrast Estimation by Beam Size Measurements

Since the offline contrast measurement does not have enough accuracy, contrast estimation using the electron beam is necessary. The following methods are only applicable after the ATF2 beam is available.

#### 5.3.1 Contrast Estimation of Small Crossing Angles

The contrast estimations of the small crossing angle modes are relatively easy if the small electron beam size is obtained. When the smaller beam size than the measurable range is arrived, the obtained modulation depth is  $\sim 100\%$ . Then, if the fringe contrast is degraded, the degradation is directly observable by the measurement. Practically, minimum fringe contrast is obtained by measuring the same beam size by two crossing angles, using a relation shown in Fig. 2(right).

In this method, the estimation of the modulation degradation is efficient if the electron beam size is reduced to the efficient range of the larger crossing angle modes. In different words, the estimation of the  $2^\circ$  mode needs  $\lesssim 1 \mu\text{m}$  electron beam size, that of the  $8^\circ$  mode needs  $\lesssim 300 \text{ nm}$  beam size, and that of the  $30^\circ$  mode needs  $\lesssim 70 \text{ nm}$  beam size. Degradation of the  $174^\circ$  mode cannot be estimated by this method because there are no larger crossing angle modes and the modulation depth cannot be high enough because the ATF2 cannot supply such a small beam size.

However, if the obtained modulation degradation is almost zero for the rest of the modes, or at least the degradation is almost the same for the modes, the degradation of the  $174^\circ$  mode is assumed to be mostly the same. Since this method can accurately acquire the degradation for the smaller angle modes, it can be a help to assume the degradation of the  $174^\circ$  mode.

#### 5.3.2 Estimation of the $174^\circ$ Mode

The previous method cannot estimate the modulation degradation of the  $174^\circ$  mode (but only can ‘assume’ the degradation). If we can acquire several beam sizes whose ratio can be estimated without data of the Shintake

monitor, we can acquire the modulation degradation by measuring the beam sizes.

The ratio of the modulation depth of two beam sizes can be written as,

$$\frac{M_1}{M_2} = \frac{M_{\text{deg}} |\cos 2\phi| \exp[-2(k_y \sigma_{y1})^2]}{M_{\text{deg}} |\cos 2\phi| \exp[-2(k_y \sigma_{y2})^2]} \quad (18)$$

$$= \exp[-2k_y^2(\sigma_{y1}^2 - \sigma_{y2}^2)] \quad (19)$$

$$= \exp \left[ -2k_y^2 \sigma_{y1}^2 \left\{ \left( \frac{\sigma_{y2}}{\sigma_{y1}} \right)^2 - 1 \right\} \right] \quad (20)$$

where  $M_{\text{deg}}$  is the contrast degradation factor.

If we know the ratio of the two beam sizes  $\sigma_{y2}/\sigma_{y1}$  and using the measured ratio of the modulation depth  $M_1/M_2$ , we can obtain  $\sigma_{y1}$  by (20). Since this method is independent of the modulation degradation  $M_{\text{deg}}$ , we can acquire the  $M_{\text{deg}}$  by the normal calculation (1) using  $\sigma_{y1}$  obtained by this method. The  $M_{\text{deg}}$  is thought not to be fluctuated time by time, so if we measure  $M_{\text{deg}}$  once, the obtained value should be used for a long period.

To perform this measurement, the beam size ratio  $\sigma_{y2}/\sigma_{y1}$  must be needed. One possibility is to change the electron beam emittance. Since the electron beam size is proportional to  $\sqrt{\text{emittance}}$  everywhere in the beam line, the emittance ratio between two electron beams are easily measured by measuring beam sizes by traditional BSMs where the beam size is much larger than the IP. The beam size larger than 10  $\mu\text{m}$  can be measured with accuracy around 1%.

If we assume that the 50 nm and 75 nm beam size with relative beam size known by 1.4% accuracy (corresponding to 1% for each), the estimation error of the  $M_{\text{deg}}$  comes 3.5%, which is in allowable range of the Shintake monitor.

## 6 Background in the Gamma Detector

Background of the gamma detector is crucial for the modulation resolution. Estimation of assumed background, its effect on the measurement, and strategy to suppress the background are discussed in this section.

### 6.1 Background Sources

#### 6.1.1 Synchrotron Radiation from Final Focusing Magnets

Electron beam passing through final focusing magnets is the main source of the synchrotron radiation for our detector. Energy spectrum of synchrotron radiation is characterized by “critical energy”, which is 1.1 keV in ATF2 assuming 1 Tesla magnetic field. Since energy distribution of the synchrotron radiation photons is limited up to several times the critical energy, all of the photons from synchrotron radiation must be stopped at the beam pipe (1.6 mm thick made of SUS304) and do not arrive at the detector.

#### 6.1.2 Beam Scattering with Residual Gas

Since the vacuum in the accelerator beam pipe is not perfect, some of the electron beam can be scattered by residual gas in the beam pipe. The amount of scattering must be estimated. Since Rutherford scattering is adiabatic and does not emit photons, we need to consider only bremsstrahlung process.

Cross section of the bremsstrahlung of an electron interacting with the residual gas for  $> 1.3$  keV photon emission (fraction of  $1 \times 10^{-6}$  from the beam energy) is estimated to be

$$\sigma_b = 2.5 \times 10^{-22} [\text{cm}^2] \quad (21)$$

assuming  $\text{N}_2$  gas[10].

The critical section for the photon emission is between the last bending magnet before the final focus area and the bending magnet after the IP ( $L \sim 1200$  [cm]), and pressure in the ATF2 beam line is lower than  $10^{-6}$  [Pa], corresponding to gas density of  $n_{\text{gas}} = 2.7 \times 10^8$  [particles/cm<sup>3</sup>].

The calculated number of scattered photons per bunch ( $n_e = 1 \times 10^{10}$ ) is,

$$n_\gamma = \sigma_b L n_{\text{gas}} n_e \sim 0.8 \quad (22)$$

which is negligible because number of signal photons is over  $10^3$  per bunch.

### *6.1.3 Beam Halo Scattering with Beam Pipe*

Charge distributions of accelerator beams can be separated to two parts, beam cores which usually have Gaussian-like distributions, and beam halos which have much broader distributions than beam cores. Diameters of beam transportation pipes are designed so that the beam core does not hit the beam pipes. However, in some parts of ATF2 beam line, beam size is enhanced by the optics and a part of the beam halo can hit the beam pipes, which emit bremsstrahlung photons.

Energy distribution of this background is already shown in Fig. 8. Since photon energy of this background is very large, we need to consider effects of the background seriously if amount of the background is not negligible. To estimate this background, we measured charge distribution of a beam halo in current ATF extraction line. The measurement result is described in the next subsection.

### *6.1.4 Particles from Beam Dump*

Since a beam dump is located close to the IP in the ATF2, it can be a large background source. Amount of detected background from the beam dump depends largely on the detector location. Since most of particles from the beam dump are backscattered ones to the upstream of the beam line, we can install the detector behind the beam dump to suppress this background.

## *6.2 Distribution of the Beam Halo*

Understanding charge distribution of the beam halo is essential to our estimation of background. As the construction of the ATF2 beam line is not completed yet, we measured the distribution at current ATF extraction line which is located upstream of the new ATF2 line. The measurement was performed in ATF spring run of 2005.

### *6.2.1 Measurement Setup*

We use wire scanners installed in the ATF2 extraction line for the scattering target. The wire scanner consists of a metal wire (tungsten in the ATF) with a micromover to scatter the electron beam at every wire position. The scattered photons are counted by a gamma detector, which is an air-Cherenkov counter

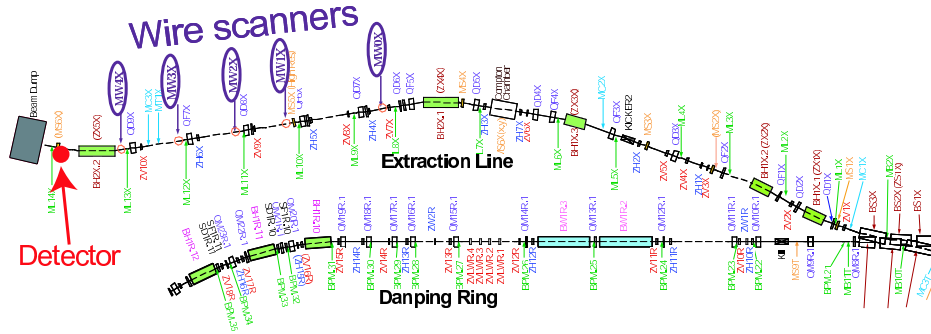


Fig. 24. Location of wire scanners and their detector in ATF extraction line.

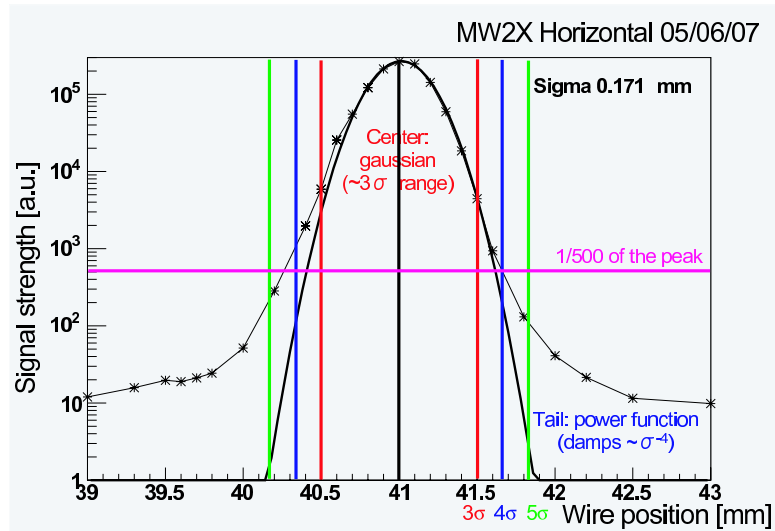


Fig. 25. Measured result of charge distribution using an ATF extraction line wire scanner.

with a 2 mm thick lead converter and a PMT is attached for the photon counting.

Figure 24 shows the location of wire scanners and a gamma detector. Five wire scanners are installed, while all of them are read by a single detector. Since electron beam size at each wire scanner is varied, we use all detectors to obtain the halo charge distribution of the various beam size.

### 6.2.2 Measurement Result

A result of the measurement is shown in Fig. 25 and Fig. 26. Figure 25 shows a measurement of charge distribution of wide dynamic range. An applied voltage of PMT is varied to obtain wide dynamic range. The plot shows that the distribution in the beam center of  $< 3\sigma$  range is well approximated by a Gaussian (bold line), while in the region of  $> 3\sigma$ , the deviation from the central Gaussian is large. Figure 26 shows a comparison of the halo distribution for several beam sizes. In the upper graph horizontal axis is in a unit of beam



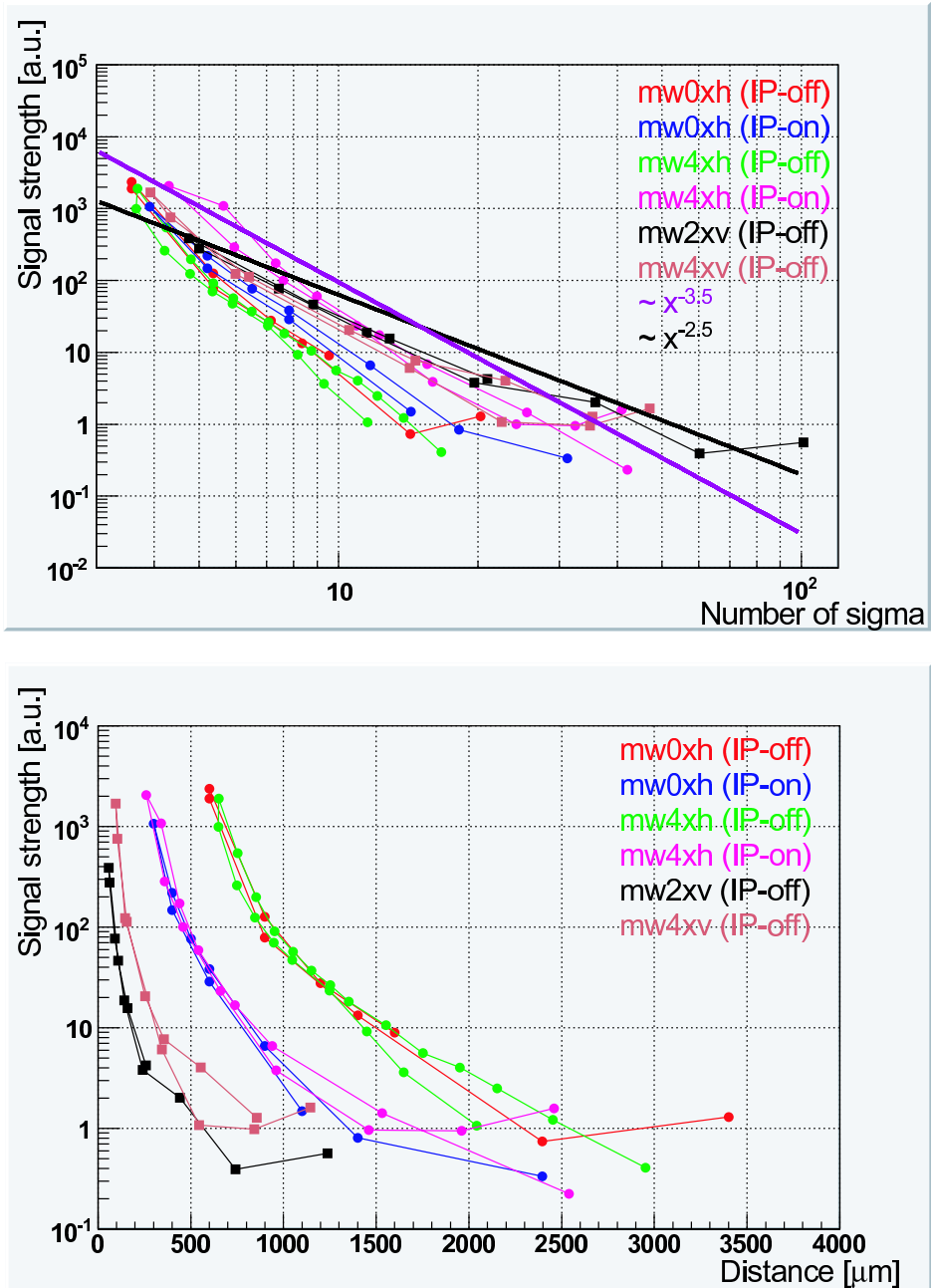


Fig. 26. Measurement of the halo part using several wire scanners for both vertical and horizontal directions. Upper graph shows the plot in which horizontal axis is normalized by its beam size. Lower graph shows the plot in which horizontal axis is just a distance from the beam center. For both graphs, vertical beam profiles are shown as a square, and horizontal beam profiles are shown as a circle. The difference of the IP-on data and the IP-off data is the vacuum level. For the IP-off data, some of the ion pumps in the ATF dumping ring were turned off to obtain data with degraded vacuum. The difference of the vacuum level is about 1:5.

size, and in lower graph it is in a absolute distance. Comparing two graphs, we can understand a width of the halo expansion is almost proportional to the center beam size.

In the upper graph of the Fig. 26, two straight line are also shown. The blue line shows a function of the  $-3.5$ th power of the distance from the center, and the black line shows a function of the  $-2.5$ th power. According to the graph, for the horizontal distribution  $-3.5$ th power is more likely to the data, while for the vertical distribution  $-2.5$ th power is more likely for  $> 6 \sigma$  region.

### 6.2.3 Estimation of Amount of Beam Halo

We can estimate the maximum charge distribution of the beam halo using the halo measurement. We assume that the halo distribution of both vertical and horizontal follow to the  $-3.5$ th power function until  $6 \sigma$ , and for outside  $6 \sigma$  the vertical distribution follows to the  $-2.5$ th power function while the horizontal distribution still follows to the  $-3.5$ th. The ratio of the charge intensity between the central Gaussian and halo function is determined so that the density of the center is 500 times larger than the density at the  $5 \sigma$  position. This value is extracted from Fig. 25.

Since the most of the charge in a bunch is concentrated in the central Gaussian, density at the center  $\rho_c$  can be easily obtained as

$$\rho_c = \frac{N}{\sqrt{2\pi}\sigma}, \quad (23)$$

where  $\sigma$  is the beam size of the central Gaussian and  $N$  is the bunch population, which is assumed to be  $1 \times 10^{10}$  electrons in this calculation. Since we assume the density of the  $5 \sigma$  is  $1/500$ , which corresponds to  $8.0 \times 10^6$  divided by the  $\sigma$ .

The result of the calculation shows that

$$\rho_{h1} = 2.2 \times 10^9 \times x^{-3.5} \quad (\text{horizontal and vertical until } 6 \sigma) \quad (24)$$

$$\rho_{h2} = 3.7 \times 10^8 \times x^{-2.5} \quad (\text{vertical outside } 6 \sigma) \quad (25)$$

where  $x$  is the distance from the beam center as a unit of  $\sigma$ . Figure 27 shows the functions. This estimated charge population is used in the following discussions.

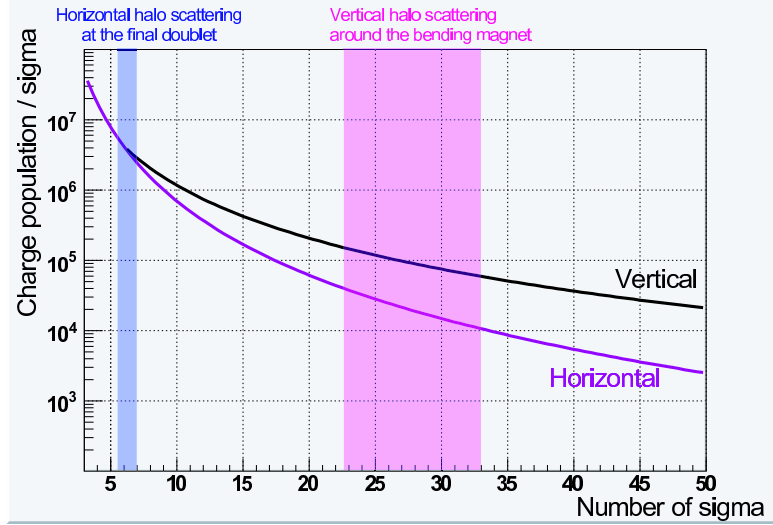


Fig. 27. Maximum charge density of the beam halo estimated by the halo measurement. Blue and purple area shows the concerned region, discussed in Section 6.2.4.

#### 6.2.4 Considerations for Beam Optics

According to the previous section, distribution of the beam halo is power functional, and the halo expansion is proportional to the central beam size.

Figure 28 shows plots of beam parameters at each components. Aperture diameter of the beam pipe is limited to 20 mm by QBPM (Quadrupole Beam Position Monitor)s equipped with every quadrupole magnet.

In the final focusing section (hatched in pink), beam size is extremely large, especially in horizontal and the aperture is very small with respect to that. To avoid large amount of background produced at that section, special QBPMs with double aperture (40 mm) will be installed in this section.

The aperture at the final focusing magnets are still too small to avoid all of the beam halo even if we use 40 mm diameter QBPMs. However, we can see sections which have smaller aperture, around  $s = 60 - 75$  m. Most of the beam halo is cut by this section and almost no halo particles are scattered in the final focus section.

Practically, we assume that small number of electrons may pass through the collimators and hit the pipe at the final focus section. The maximum number of the electrons in  $5.5 - 7 \sigma$  region is estimated to be around  $5.6 \times 10^6$  using (24), and we assume  $1.0 \times 10^6$  electrons remained and scatter with the final doublet.

Another problem exists in downstream of the IP. The final focusing magnets strongly focus the electron beam with large focusing angle towards the IP, and

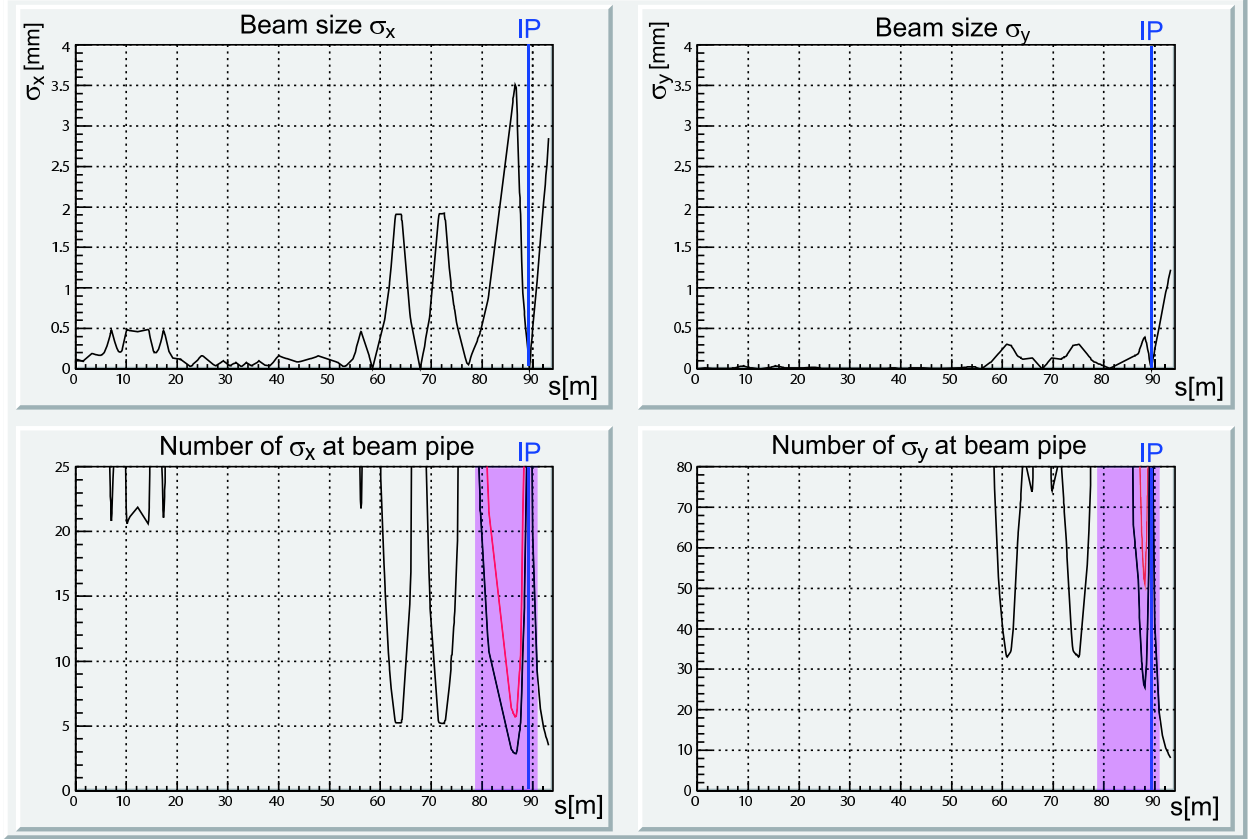


Fig. 28. Upper: beam size plot in the planned ATF2 line. Horizontal axis shows  $s$ [m], which is a distance along the beam path from the entrance. Left plot shows horizontal beam size, and right plot shows vertical. Lower: Number of  $\sigma$  at a beam pipe of each components. Diameter of the beam pipe is fixed to 20 mm in this plot. The red line at the final focus section shows a case of 40 mm diameter. The pink area shows a straight section around the IP, where produced background can geometrically reach the Shintake gamma detector.

the large focusing angle causes large beam size after the IP. This results in the large background from around the bending magnet after the IP.

Since the aperture at the middle of the bend is around  $22.5 \sigma$ , we assume  $1.0 \times 10^6$  electrons, which is calculated by integrating (25) from  $22.5$  to  $33 \sigma$ .

The number of halo electrons assumed to produce background are much larger than the number of signal photons. The background must be eliminated by an appropriate photon collimator installed in front of the gamma detector, as described in the next subsection.

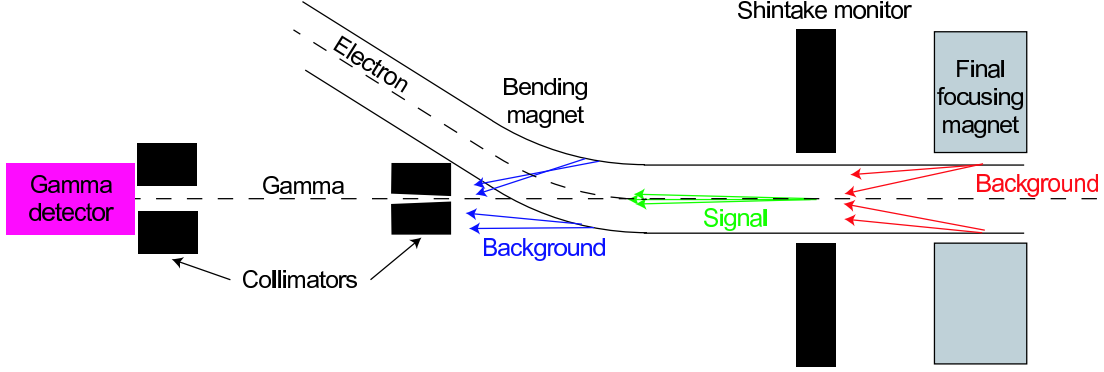


Fig. 29. A schematic of position of the gamma collimators.

### 6.3 Gamma Collimator

We will install gamma collimators in front of the gamma detector to reject background. Figure 29 shows a schematic of the geometry. Background photons are assumed to be produced at the final focusing magnet (shown as red arrows), and at the bending magnet (as blue), while signal is produced at the IP (as green).

Since distribution of the Compton signal is like a point-source and dispersion angle is smaller than background, cone-shape collimators can efficiently select signal photons. Origin of the cone is set at the IP.

Opening angle of the cone is decided by comparing acceptance for signal and background photons. We use three opening angles in the background estimation study. The selected opening angles are shown in Table 4 with calculated signal acceptance and estimated amount of background. The collimator is located 3.0 m from the IP, which is just behind a beam pipe of the bending magnet crossing the gamma beam line.

Acceptance of the gamma collimator for the background photons is estimated using a GEANT4 simulation. The acceptance for the photons from the final doublet and that from around the bending magnet are separately investigated.

The result for the photons from the final doublet is shown in Fig. 30(a). In this simulation, initial electrons hit the beam pipe at the final doublet and we monitor the energy deposit of the photons at the detector, passing through a gamma collimator. The plot shows the energy spectra of the arriving photons passing through collimators of several apertures.

The acceptance for the background from around the bending magnet is shown in Fig. 30(b). In this simulation, initial electrons come from the IP with vertical angles from 3 to 10 mrad. from the beam axis. The vertical angles is projected to the horizontal axis of the plot. The horizontal dispersion is not introduced

Setup. no.	Opening angle	Signal acceptance	Final doublet BG acceptance	Bending magnet BG acceptance	Estimated BG photons
1	2.20 mrad	95%	0.507%	3.64%	41000
2	1.30 mrad	80%	0.060%	0.04%	1000
3	0.83 mrad	60%	0.004%	< 0.02%	< 500

Table 4

Opening angles of assumed gamma collimators with the energy acceptance and the amount of background estimated by simulations. For estimating number of total background photons  $10^6$  initial bremsstrahlung photons are assumed for background amount of both from final doublet and from bending magnet.

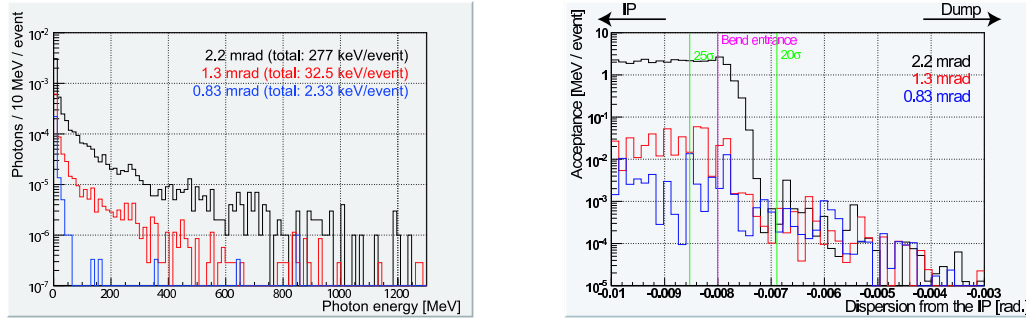


Fig. 30. (a) A simulation result of the acceptance of the background photons emitted around the final doublet. Arrived energy spectra for the three collimator setups are shown. The vertical axis stands for an arrived number of photons in a 10 MeV bin width per 1 electrons scattering the final doublet. (b) A simulation result of the acceptance of the background photons emitted around the bending magnet downstream the IP.

because the horizontal beam halo is tightly cut by the forward apertures, while in the vertical it is cut only at 33 sigma.

The green lines show the angles corresponding to the specified number of sigma, which is calculated from the vertical beam dispersion of the beam core (0.343 mrad.) from the IP. The pink line shows the entrance of the bend. Downstream the bend, the acceptance is strongly suppressed because the electron beam is swept out from the gamma beam line. Three histograms show the variation by the collimator aperture.

Practically the amount of the background may vary from the estimation, and we can choose a proper aperture by monitoring the background level.

#### 6.4 *Effects of the background*

Since the amount of background is not modulated by varying phase of the interference fringe, the background decreases modulation depth and can be a systematic error of the modulation measurement. However, we can obtain pure-background signal at the detector by switching off laser pulses. If we set the laser pulse interleaved (which means we only fire a laser pulse for every two electron bunches), both “signal+background” and “background only” data are obtained. “Signal only” data can easily be obtained by merely subtracting “background only” data from “signal+background” data. By this way, systematic effect to the modulation depth is perfectly eliminated.

Statistical fluctuation to the modulation spectra is remained due to the arbitrary fluctuation of the background amount. The rightmost column of Table 4 summarises estimated amount of background for three collimator setups. We should take into account two considerations:

- Average background photon energy is 3.7 times larger than average signal photon energy. (Dependence of average background energy on collimator setups is small.)
- Energy deviation of the individual photons should be considered. Statistical fluctuation is 2.9 times larger than  $\sqrt{N}$  ( $N$  is number of background photons).

Since the amount of background in Setup 1 is too large, we adopt Setup 2 (number of BG = 1000) for resolution estimation, discussed in the next section.

Error source	Jitter (uncorrected)	Jitter (corrected)
Electron bunch population	7.5% (sample)	1%
Laser Peak Power	4.1%	3.8% (integral correction)
Laser Timing	< 1%	-
Laser Spot Size	1%	-
Laser Beam Position	3.9%	1.4%
Total	-	~ 4.4%

Table 5  
Summary of error sources of intensity jitters.

## 7 Performance of Shintake Monitor

In this section resolution and accuracy of the Shintake monitor is discussed using error estimations described in former sections.

### 7.1 Sources of Statistical Fluctuations

Several types of sources cause fluctuations in the modulation measurements for the Shintake monitor. In this section the amount of the fluctuations is estimated for each source.

#### 7.1.1 Intensity Jitters

Intensity jitters cause random fluctuations to each data point in the modulation spectra. The average amount of jitters of this type is assumed to be proportional to the signal strength.

Various error sources cause this type of error, including laser power jitter, laser position jitter, laser timing jitter, electron beam bunch population etc. Some part of the intensity jitters can be canceled out using results of individual measurements of error sources.

Table 5 is a list of error sources classified to the intensity jitters. With proper correction, the total fluctuation to each measurement point is  $\lesssim 4.4\%$ .

Statistical fluctuations of measured number of photons in the detector causes similar fluctuation to the modulation spectra, but the amount of fluctuations of this type is not proportional to the signal strength but proportional to  $\sqrt{\text{thesignalstrength}}$ . However, since the average number of photons is about



3000 in expected condition, the statistical fluctuations are less than 1%, negligible compared to other sources.

### 7.1.2 *Phase Jitters*

As discussed in Section 4, fluctuation of the laser fringe phase where the electron beam passes is one of the critical error sources. This type of error causes horizontal fluctuations for individual data points in the modulation spectra.

Both fluctuations of laser fringe and electron beam position cause this error. The amounts of errors are already estimated as 10.1 nm (fringe) and 8.7 nm (electron) after corrections. The combined amount of error is 13.3 nm.

### 7.1.3 *Background Jitters*

Fluctuation of the amount of background causes imperfect background subtraction. By assuming that number of background photons arrived at the detector fluctuates only by statistics, we can estimate the effects to the modulation plots. The average number of arrival photons is estimated to be 1000 with Setup 2 of Table 4. Considering discussions in Section 6.4, average fluctuation of background in unit of average signal energy (53 GeV/bunch, 4400 photons/bunch  $\times$  80% (collimator acceptance)  $\times$  15.11 MeV/photon (average energy of Compton photons) ) is about 9.7%.

Note that the background estimation is based on the worst case. Practically the number of beam halo may be smaller and the amount of background may also be smaller.

## 7.2 *Statistical Resolution of Shintake Monitor*

In this section, Shintake monitor is assumed to use 45 electron bunches for beam size measurements. This corresponds to about 1 minute (including bunches for background subtraction), which is considered to be reasonable period. To reduce statistical fluctuation longer measurement period is preferred, but slow drifts (electron beam position shift, beam size shift, etc.) might be critical for long-term measurements.

To interpret individual statistical fluctuations to resolution of the beam size measurement, we use a toy Monte Carlo simulation. The simulation scheme is:

- (1) Making a “modulation plot”, which is a set of measurement points. A measurement point simulates a signal intensity at a certain fringe phase, including errors (random fluctuations) discussed in the previous subsection. In the modulation plot, the fringe phase is changed point by point, and the scanning manner depends on the measurement method (discussed later). A simulated modulation depth is also acquired by the method using the plot.
- (2) Repeating making modulation plots and obtaining a histogram of the simulated modulation depths. Deviation of the simulated modulation depths stands for the resolution for modulation measurements.
- (3) Repeating those for various (true) modulation depths and measurement methods.

As measurement methods, we use following three methods.

- Fitting Method

The fringe phase is scanned via fixed steps over a period. We fit the obtained spectrum by a sine curve with free parameters of amplitude, offset, and phase and the amplitude is used as a modulation depth.

- RMS Method

Scanning of the fringe phase is the same as the fitting method. Evaluation of the modulation depth is not by fitting but merely getting RMS value of the scanning spectrum.

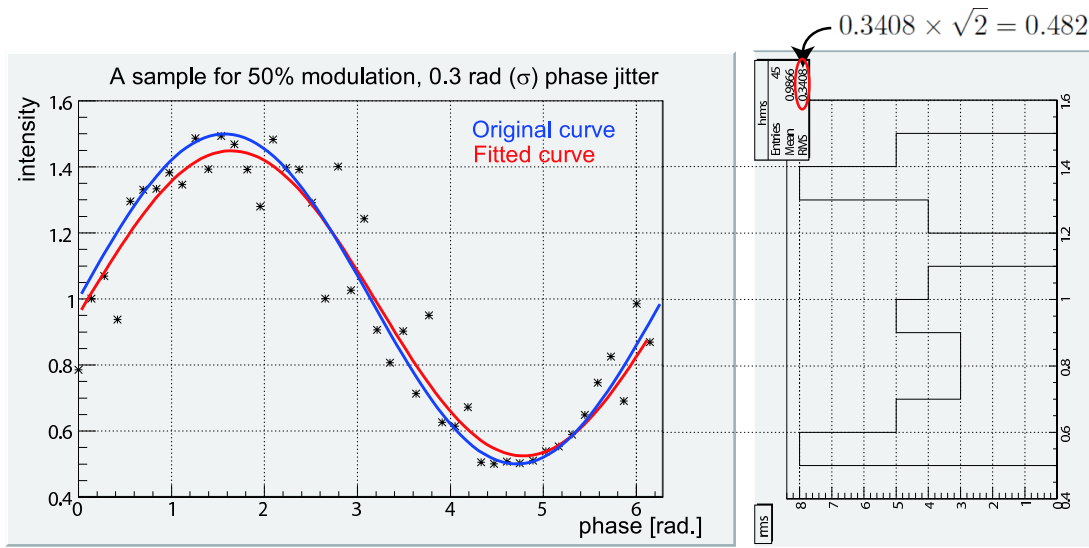
- Peak Search

Peak search method consists of two stages of measurements. First stage consists of 25 points, obtaining the peak position of the modulation. In this stage the fringe phase is scanned linearly, as same as previous methods and fitting by a sine curve is applied immediately after scan.

In second stage we measure the intensity at the top and the bottom of the modulation (each 10 points), using the phase information obtained in the first stage. Measured top and bottom data are averaged respectively, to calculate the modulation depth. First stage data taken at the peak search are not used in the modulation estimation.

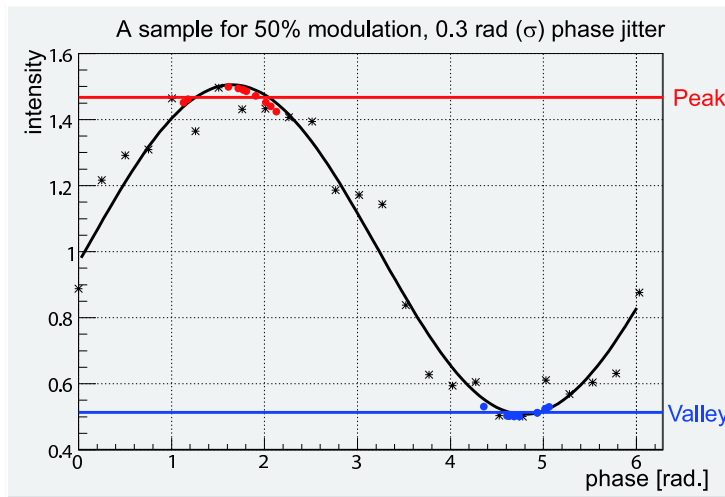
Figure 32 shows a dependence of the statistical uncertainty of the measured modulation depth on each method. The fitting and the RMS method give similar results, while the RMS method gives slightly smaller uncertainty, especially for the small modulation region. Peak search gives better result than other two methods in the range of large modulation depth, while it is worse than the RMS method in the modulation depth less than 35%.

Our goal is to obtain 3% resolution within the observable range. With the peak search method, both of the goals can be achievable if the assumed error conditions are real. Practically, the peak search method is used for  $M > 35\%$  measurements and the RMS method is used for  $M \leq 35\%$  measurements to



Fitting method

RMS method



Peak search method

Fig. 31. Schematics of the measurement methods. Top-left: the fitting method. Obtained modulation plot is fitted by a sine function to obtain the modulation depth. Top-right: the RMS method. Modulation points are projected, and obtain RMS value to be interpreted to the modulation depth. Bottom: the peak search method. First 25 points are used to obtain peak position, and subsequent 20 pulses are used to obtain the intensity at the peak and the valley phase.

obtain the best resolution.

Figure 33 shows the estimated beam size resolution using the peak search at  $M > 35\%$  and the RMS method at  $M \leq 35\%$ . From the plot, we conclude that the 10% resolution over the observable beam size range from 25 nm to 6

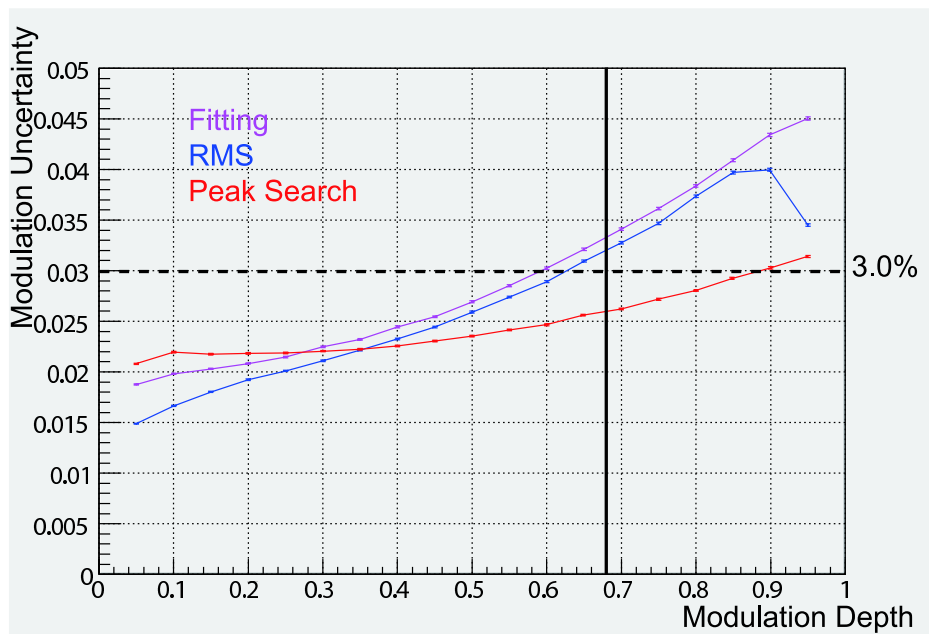


Fig. 32. Plot of modulation uncertainty vs. modulation depth on each method. Power, phase and background jitter, whose amount is described in the text, are included. Error bars (hardly seen) stand for the error caused by limited statistics of the simulation. The suppression of the RMS method in  $M \geq 0.9$  region is due to saturations of the measured modulation depth at  $M = 1$ .

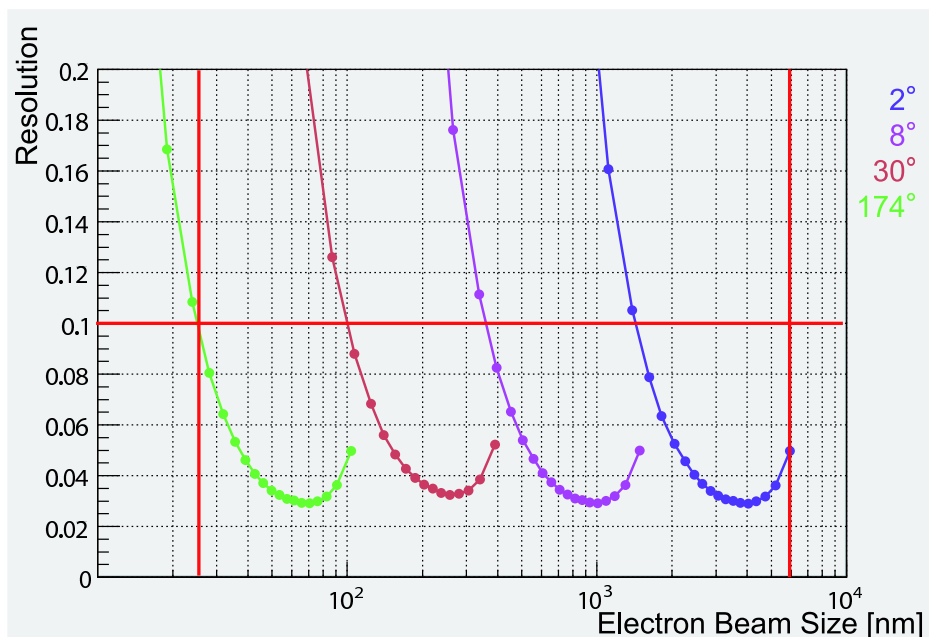


Fig. 33. The estimated beam size resolution. For the 25 - 6000 nm beam size, target resolution 10% can be achieved using 2°, 8°, 30° and 174° crossing angle modes.

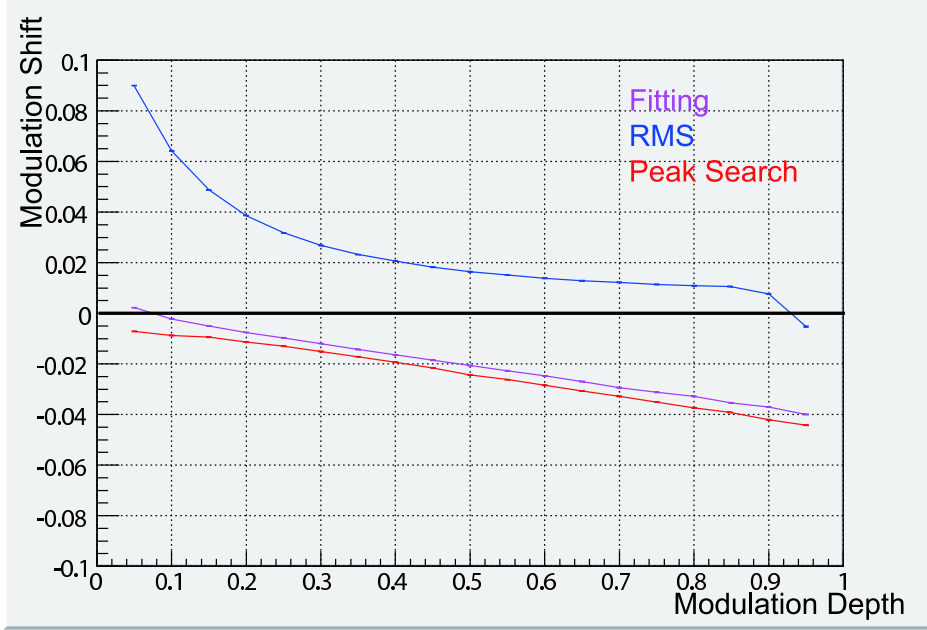


Fig. 34. Plot of average modulation shift on each method. Amount of jitters is the same as Fig. 32. The depression of the RMS method at  $M = 0.95$  is due to the saturation effect similar to Fig. 32.

$\mu\text{m}$  can be achieved.

### 7.3 Systematic Errors

For 37 nm beam size measurement, suppression of the systematic error is important. The target accuracy of the beam size measurement is  $37 \pm 2$  nm, which corresponds to  $68 \pm 2.8\%$  modulation depth in the  $174^\circ$  mode.

The expected sources of the systematic effects are (1) average modulation shift caused by the random fluctuations (discussed previously), and (2) imperfect fringe contrast discussed in Section 5. We need to suppress both effects to obtain desired accuracy.

#### 7.3.1 Cancellation of the Average Modulation Shift

The average modulation shift can be estimated by the same Monte Carlo simulation as used in the previous subsection.

Figure 34 shows average shifts of modulation measurements by each method. In the fitting and peak search method, phase jitter causes a negative shift for the obtained modulation depth, and in the RMS method intensity jitter causes a positive shift for the obtained modulation depth.

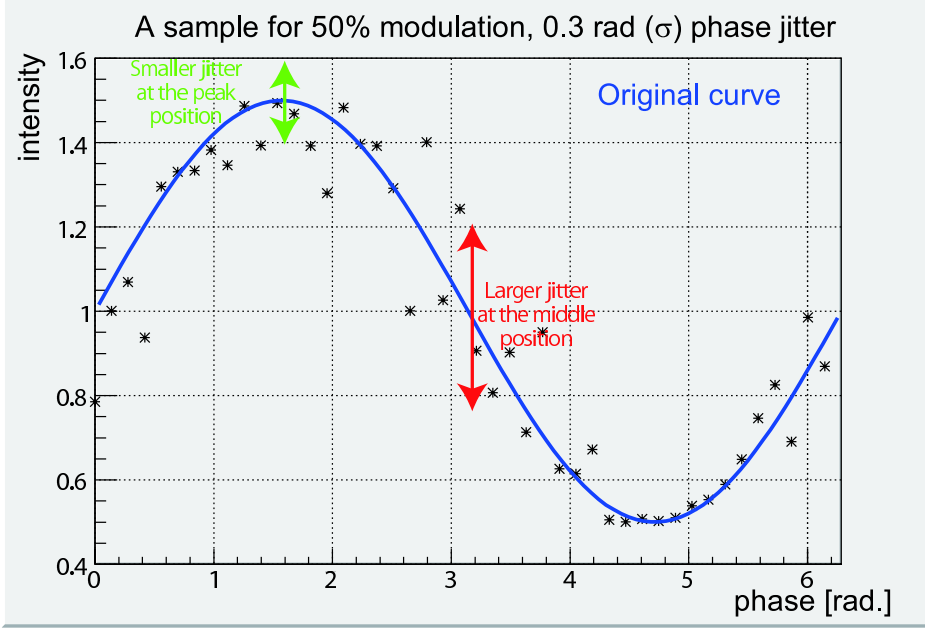


Fig. 35. A sample of the modulation plot with 0.3 radian phase jitter. The power deviation with respect to the original curve is larger in the “middle position” than the “peak position”. Therefore, the middle position can be used to obtain the phase jitter.

Since the 37 nm beam size measurement corresponds to 68% modulation depth in the 174° mode, we need to correct the shift in the peak search method. The average modulation shift of the peak search method can be expressed as,

$$\delta_M = \frac{M}{\sqrt{2\pi}\sigma} \int_{-\infty}^{+\infty} \exp\left(-\frac{x^2}{2\sigma^2}\right) \cos x dx - M \quad (26)$$

$$\simeq -\frac{\sigma^2 M}{2} \quad (\sigma \ll 1) \quad (27)$$

where  $\sigma$  is the average phase jitter. If we can obtain the amount of phase jitter, the shift can be corrected.

The amount of the phase jitter can be observed by following steps.

- (1) Acquiring background fluctuation by accumulating “laser-off” pulses.
- (2) Accumulating data with single-path light. The data include “power jitter” in addition to the background fluctuation.
- (3) Measure the data with the fringe phase of the “middle position”, shown in Fig. 35. The power fluctuation due to the phase jitter is enhanced at the middle position.

The required accuracy of the phase jitter for the  $37 \pm 2$  nm beam size measurement can be calculated using (27) as,

$$\Delta\delta_M \equiv \delta'_M - \delta_M = -\frac{(\sigma'^2 - \sigma^2)M}{2} \quad (28)$$

$$\Delta\sigma \equiv \sigma' - \sigma \simeq \frac{\Delta\delta_M}{M\sigma} \quad (29)$$

where  $\Delta\delta_M$  is the accuracy of the modulation depth and  $\Delta\sigma$  is the accuracy of the phase jitter. Assigning  $M = 0.68$ ,  $\sigma = 0.31$  [rad.] and  $\Delta\delta_M = 0.028$ , we obtain  $\Delta\sigma = 0.137$  [rad.], which is 46% of the  $\sigma$ . This resolution of the  $\sigma$  can be easily obtained by using 20 bunches for the “middle position” measurement (actually the resolution of the  $\sigma$  is estimated to be 16% by 20 bunch measurement).

With this correction, the systematic shift is converted to the statistical fluctuation, caused by the resolution of the phase jitter. The overall statistical error for the 37 nm beam size measurement is modified from 2.6% (see Fig. 32) to 2.8%, corresponding to 2.0 nm resolution on the beam size.

### 7.3.2 Treating Fringe Contrast Degradation

As described in Chapter 5, the fringe contrast cannot be estimated with the required accuracy. The current estimation is  $M_{\text{deg}} < 77\%$ , which has an unacceptable uncertainty, and even the measurement result is not consistent with the estimation.

For a practical estimation of the fringe contrast, measurements with the ATF2 beam are indispensable. As discussed in Section 5.3, the fringe contrast can be measured with the accuracy of 3.54% by the measurement of the modulation ratio. For measurements of the 68% modulation depth, the modulation error is  $3.54\% \times 0.68 = 2.4\%$ .

### 7.3.3 Conclusion

I conclude that the beam size measurement of the 37 nm ATF2 electron beam can be performed using the Shintake monitor by,

- 2.8% modulation resolution, corresponding to 2.0 nm beam size,
- 2.4% accuracy, corresponding to 1.7 nm beam size,

when the assumed conditions are achieved at the actual beam line.

## 8 Summary and Prospects

Shintake monitor is a nanometer electron beam size monitor using a laser interference fringe formed by two split laser beams crossing at the electron beam path. Our monitor is planned to measure 25 nm to 6  $\mu\text{m}$  vertical beam size by  $2^\circ$ ,  $8^\circ$ ,  $30^\circ$  and  $174^\circ$  switchable crossing angles, and 2.8 to 100  $\mu\text{m}$  horizontal beam size using laser beam scanning (laser-wire) method in the ATF2 focal point.

Concept, overall layout, critical technical issues such as phase stabilization, beam position stabilization, fringe contrast and background of the detector are discussed in this paper. The estimated performance is less than 10% resolution in all measurement range 25 to 6  $\mu\text{m}$  in 1 minute measurements, and less than 2.0 nm accuracy at 37 nm ATF2 design beam size. This performance meets the requirements to achieve goals of the ATF2 experiment. ATF2 operation will start at this October. Until summer 2009, ATF2 is planned to achieve sub- $\mu\text{m}$  beam size and the first beam size measurement by the Shintake monitor will be performed.

Shintake monitors can be useful for the real-ILC beam tuning. For using in the ILC, several consideration should be needed.

- Because the beam energy of the ILC is much larger than the ATF2, the cross section of Compton scattering is lower, about 1/10 of the ATF2. We need more laser beam intensity or stronger laser focusing to maintain the signal strength of the gamma detector.
- As the peak energy of the Compton scattering photons is almost the same as beam energy, energy separation of signal and pipe-scattered background is not realistic. In addition, the energy of synchrotron radiation photons from focusing magnets is also larger in ILC, which should be cut by some kind of shields in front of the gamma detector.
- The IP beam size of the ILC is 5.7 nm. For measuring 5.7 nm beam size, wavelength of the laser beam should be minimized. In commercially available lasers, 193 nm excimer laser may be minimum for high power pulsed beam. Using a 193 nm laser, 5 nm measurement is not impossible. Assuming the same resolution of the modulation depth measurement as the ATF2 goal, the resolution on beam size is about  $\pm 1$  nm (18 %).
- If the Shintake monitor is used for the IP beam size monitor in a tuning stage, it needs a space for the optical table at the IP. Since the ILC detector cannot be placed during the tuning with the Shintake monitor, a replacement structure such as a push-pull system must be needed.



## Acknowledgments

The authors thank J. Urakawa, N. Terunuma and ATF collaboration for useful discussions and facility support. T. Shintake, H. Matsumoto and A. Hayakawa, designers and manufacturers of the FFTB Shintake monitor provided us useful material and comments based on their former experience. M. Ross, D. McCormick, T. Okugi and other SLAC people gave us much help for shipping FFTB Shintake monitor components to Japan to be utilized in the ATF2 Shintake monitor. This research was supported by Joint Japan-US Collaboration in High-Energy Physics.

## References

- [1] J. Brau *et al.*, International Linear Collider Reference Design Report, arXiv:0712.1950 (Vol. 1), arXiv:0709.1893 (Vol. 2), arXiv:0712.2361 (Vol. 3), arXiv:0712.2356 (Vol. 4).
- [2] C. Field, Nucl. Inst. and Meth. **A360** (1995) 467.
- [3a] T. Shintake, Nucl. Inst. and Meth. **A311** (1992) 453.
- [3b] P. Tenenbaum and T. Shintake, Annu. Rev. Nucl. Part. Sci. **49** (1999) 125.
- [4] T. Suehara, Doctor thesis at the Univ. of Tokyo (2008).
- [5a] M. Berndt *et al.*, Final Focus Test Beam Project Design Report, SLAC-REP-376 (1991).
- [5b] V. Balakin *et al.*, Phys. Rev. Lett. 74, 2479 (1995)
- [6] T. Shintake *et al.*, Proc. PAC 1995, Dallas, USA, Vol. 4, pp. 2444.
- [7] ATF2 Collaboration (B. Grishanov *et al.*), ATF2 Proposal, KEK Report 2005-2.
- [8] H. Yoda, Master thesis at the Univ. of Tokyo (2008).  
Journal paper is in preparation.
- [9a] Y. Honda *et al.*, Development of high resolution cavity beam position monitor, in preparation.
- [9b] T. Nakamura, Master thesis at the Univ. of Tokyo (2008).
- [10] A. Chao *et al.*, Handbook of Accelerator Physics and Engineering, p.258, World Scientific (1999).